

Global Structure of Optically Thin, Magnetically Supported, Two-Temperature, Black Hole Accretion Disks

Hiroshi ODA¹, Mami MACHIDA², Kenji E. NAKAMURA³, Ryoji MATSUMOTO⁴, and Ramesh NARAYAN⁵

¹*Shanghai Astronomical Observatory, Chinese Academy of Sciences, 80 Nandan Road, Shanghai 200030, China*
hoda@shao.ac.cn

²*Department of Physics, Faculty of Sciences, Kyushu University 6-10-1 Hakozaki, Higashi-ku, Fukuoka, 812-8581, Japan*

³*Department of Mechanical Engineering, Faculty of Engineering, Kyushu Sangyo University, 2-3-1 Matsukadai, Higashi-ku, Fukuoka 813-8503, Japan*

⁴*Department of Physics, Graduate School of Science, Chiba University, 1-33 Yayoi-cho, Inage-ku, Chiba 263-8522, Japan*

⁵*Harvard-Smithsonian Center for Astrophysics, 60 Garden Street, Cambridge, MA 02138, USA*

(Received ; accepted)

Abstract

We present global solutions of optically thin, two-temperature black hole accretion disks incorporating magnetic fields. We assume that the $\varpi\varphi$ -component of the Maxwell stress is proportional to the total pressure, and prescribe the radial dependence of the magnetic flux advection rate in order to complete the set of basic equations. We obtained the magnetically supported (low- β) disk solutions, whose luminosity exceeds the maximum luminosity for an advection-dominated accretion flow (ADAF), $L \gtrsim 0.4\alpha^2 L_{\text{Edd}}$, where L_{Edd} is the Eddington luminosity. The accretion flow is composed of the outer ADAF, a luminous hot accretion flow (LHAF) inside the transition layer from the outer ADAF to the low- β disk, the low- β disk, and the inner ADAF. The low- β disk region becomes wider as the mass accretion rate increases further. In the low- β disk, the magnetic heating balances the radiative cooling, and the electron temperature decreases from $\sim 10^{9.5}\text{K}$ to $\sim 10^8\text{K}$ as the luminosity increases. These results are consistent with the anti-correlation between the energy cutoff in X-ray spectra (hence the electron temperature) and the luminosity when $L \gtrsim 0.1L_{\text{Edd}}$, observed in the bright/hard state during the bright hard-to-soft transitions of transient outbursts in galactic black hole candidates.

Key words: accretion, accretion disks — black hole physics — magnetic fields — radiation mechanisms: non-thermal

1. Introduction

The spectral behavior of black hole candidates (BHCs) contains valuable information on physical state of accretion disks. It is known that galactic BHCs show X-ray spectral state transitions in their transient outbursts. The system typically undergoes a transition from the low/hard state to the high/soft state (so-called hard-to-soft transition). In the low/hard state, the X-ray spectrum is approximated by a hard power law (photon index ~ 1.7) with an exponential cutoff ($E_{\text{cut}} \sim 200\text{ keV}$), and the luminosity is low. In the high/soft state, the X-ray spectrum is dominated by a blackbody component emitted from the standard accretion disk (Shakura & Sunyaev 1973), and the luminosity is high.

X-ray observations of BHCs have identified two types of hard-to-soft transition (e.g., Belloni et al. 2006; Gierliński & Newton 2006). One is the bright hard-to-soft transition whose transition luminosity is high ($\sim 0.3L_{\text{Edd}}$), where $L_{\text{Edd}} = 4\pi cGM/\kappa_{\text{es}} \sim 1.47 \times 10^{39} (M/10M_{\odot}) (\kappa_{\text{es}}/0.34\text{ cm}^2\text{ g}^{-1})^{-1} \text{ erg s}^{-1}$ is the Eddington luminosity, M is the black hole mass, and κ_{es} is the electron scattering opacity. The other is the dark hard-to-soft transition whose transition luminosity is low

($< 0.1L_{\text{Edd}}$).

In the bright hard-to-soft transition, several additional X-ray spectral states are identified during the transition from the initial low/hard state to the high/soft state: bright/hard state (or simply, the brightening of the hard state), intermediate state, and very high/steep power-law state (e.g., Homan & Belloni 2005; Miyakawa et al. 2008). The X-ray spectrum in the bright/hard state is approximated by a hard power law as in the low/hard state. However, the energy cutoff decreases from $\sim 200\text{ keV}$ to $\sim 50\text{ keV}$ as the luminosity increases (in other word, strongly anti-correlates with the luminosity) in the bright/hard state while it is roughly constant (or very weakly anti-correlates with the luminosity) around 200 keV in the low/hard state (e.g. Joinet et al. 2008; Miyakawa et al. 2008; Motta et al. 2009). In general, the energy cutoff is related to the temperature of the thermal Comptonizing electrons in an optically thin disk (or corona) close to the black hole. Spectral analyses with thermal Comptonization models (e.g. COMPST model in XSPEC introduced by Sunyaev & Titarchuk 1980, COMPTT model by Titarchuk 1994, and COMPPS model by Poutanen & Svensson 1996) also show the anti-correlation between the electron temperature and the luminosity (e.g. Joinet et al. 2008; Miyakawa et al. 2008).

In order to account for this anti-correlation, Miyakawa et al. (2008) proposed a possible scenario that the heating balances the radiative cooling due to the inverse Compton scattering; that is, the accretion flow is radiatively efficient in the bright/hard state.

In addition to the appearance of these additional states, recent analyses on the X-ray and radio data of BHCs (e.g., Fender et al. 2009) suggest that episodic ejections of relativistic jets are associated with the bright hard-to-soft transition. The episodic ejections are observed at near the peak luminosity of each outburst during the transition from the bright/hard state to the very high/steep power-law state. (Note that they are not observed in the bright/hard state). Therefore, understanding the physical mechanism in the bright/hard state may play an important role in understanding the mechanism of the disk-jet coupling in BHCs. In this paper, we focus on the physical state of the accretion disk in the bright/hard state.

The standard disk model (Shakura & Sunyaev 1973) has been widely and successfully used to account for the blackbody component. However, optically thin, hot accretion disks have been studied to account for hard X-rays from BHCs (Thorne & Price 1975; Shibazaki & Hōshi 1975). Eardley et al. (1975) and Shapiro et al. (1976) constructed a model for an optically thin, two-temperature accretion disk in which ions are much hotter than electrons and the viscous heating balances the radiative cooling. This model, however, is thermally unstable.

Advection-dominated accretion flows (ADAFs) or radiatively inefficient accretion flows (RIAFs) were introduced by Ichimaru (1977) and have been studied extensively by Narayan and Yi (1994, 1995) and Abramowicz et al. (1995). Esin et al. (1997, 1998) found that the maximum luminosity for the ADAF/RIAF is $L \sim 0.4\alpha^2 L_{\text{Edd}}$, where α is the viscous parameter (Shakura & Sunyaev 1973), and showed that the electron temperature is $T_e \gtrsim 10^{9.5}\text{K}$. Therefore, the ADAF/RIAF model can account for the high-energy cutoff and the low luminosity in the low/hard state. However, this model cannot account for the relatively low-energy cutoff ($E_{\text{cut}} \lesssim 200\text{ keV}$, hence the relatively low electron temperature) and the high luminosity ($L \gtrsim 0.1 L_{\text{Edd}}$) observed in the bright/hard state.

Luminous hot accretion flows (LHAFs) were proposed by Yuan (2001, 2003), in which heat advection works as an effective heating and balances the radiative cooling above the maximum mass accretion rate for the ADAF/RIAF. Although this model is thermally unstable, Yuan et al. (2003) concluded that the thermal instability will have no effect on the dynamics of the LHAF because the accretion timescale is shorter than the growth timescale of the local thermal perturbation at high mass accretion rates. The LHAF model can partly account for the bright/hard state observed in the range of a relatively low luminosity and a relatively high energy cutoff (e.g., Yuan & Zdziarski 2004; Yuan et al. 2007). However, this model also cannot account for the bright/hard state observed in the range of a higher luminosity and the lower energy cutoff because the electron temperature is a little too high ($T_e \sim 10^9\text{K}$). In addition, the anti-correlation between the luminosity

and the electron temperature is weak.

In these models, magnetic fields are not considered explicitly, and the plasma β ($\equiv p_{\text{gas}}/p_{\text{mag}}$) is given as a constant parameter in general (typically, $\beta \gtrsim 1$). A robust mechanism of excitation of magnetic turbulence in accretion disks is thought to be the magneto-rotational instability (MRI), since Balbus and Hawley (1991) pointed out its importance. Many local and global magnetohydrodynamic (MHD) simulations have investigated the growth and the saturation level of the MRI in accretion disks. These simulations revealed that the MRI can excite and maintain magnetic turbulence and that the Maxwell stress generated by the MRI can efficiently transport the angular momentum of the disk gas. In addition, several MHD simulations and analytical studies suggest that magnetic turbulence driven by the MRI can survive even when the magnetic pressure is dominant; therefore, highly magnetized accretion disks are astrophysically viable (e.g., Shibata et al. 1990; Pessah & Psaltis 2005; Machida et al. 2006; Johansen & Levin 2008).

Machida et al. (2006) demonstrated transitions from an ADAF/RIAF-like disk (optically thin, geometrically thick, radiatively inefficient, hot, gas pressure dominant disk; $\beta \sim 5$) to a low- β disk (optically thin, geometrically moderately thick, radiatively efficient, cool, magnetic pressure dominant disk; $\beta \sim 0.1$) by global three-dimensional MHD simulations incorporating the radiative cooling (see figure 1). When the mass-accretion rate exceeds the threshold for the onset of a cooling instability, the initial ADAF/RIAF-like disk rapidly shrinks in the vertical direction due to the cooling instability. During the transition, azimuthal magnetic fluxes inside the disk are almost conserved because the timescale of the cooling instability is shorter than that of the buoyant escape of magnetic fluxes from the disk surface. In this way, the magnetic pressure becomes dominant and supports the disk. Johansen and Levin (2008) performed vertically stratified shearing box simulations of a local patch of such highly magnetized disks. They showed that the MRI still survives even in such magnetic pressure dominant disks; thus, magnetic fields are still turbulent. Although the strong magnetic field reduces the growth rate of the Parker instability (Parker 1966) and the MRI, the generation of azimuthal magnetic fluxes around the equatorial plane still balances the buoyant escape of magnetic fluxes from the disk surface. Hence the system can stay in a quasi-steady state. We note that such low- β disks are essentially different from magnetically-dominated accretion flows (MDAFs; Meier 2005) which appear in the innermost plunging region of optically thin disks (see also figure 1. We will discuss this issue in the discussion section). We focus on the low- β disk in this paper.

Mineshige et al. (1995) suggested that an optically thin, magnetic pressure dominated disk emits hard X-rays. Pariev et al. (2003) developed a local analytical model of an optically thick, geometrically thin, strongly magnetized disk which produces spectra quite similar to those of the standard disk model. The property of such magnetically dominated disks was extensively examined

by Begelman and Pringle (2007). Bu et al. (2009) presented self-similar solutions of magnetized ADAF/RIAF.

Oda et al. (2007) constructed an one-temperature plasma model of an optically thin accretion disk incorporating magnetic fields on the basis of the results of three-dimensional MHD simulations. They assumed that the $\varpi\varphi$ -component of the stress tensor is proportional to the total pressure, and prescribed the advection rate of azimuthal magnetic fluxes in order to complete the set of basic equations of the vertically integrated, one-dimensional accretion flow in steady state. Oda et al. (2009) extended the model to an optically thick disk model and Oda et al. (2010) extended it to a two-temperature plasma model. They obtained local thermal equilibrium solutions, and found a new, thermally stable, low- β disk solution in the optically thin and thick regime. The local thermal equilibrium solution of the optically thin low- β disk exists above the maximum mass accretion rate for the ADAF/RIAF, and the electron temperature is lower than that in the ADAF/RIAF. They concluded that the optically thin, low- β disk can account for the bright/hard state during the bright hard-to-soft transition of BHCs. However, the results reported by Oda et al. (2009, 2010) were based on the local models in the sense that the interactions between adjacent annuli of the disk were neglected (or, put mathematically, the derivative terms in the basic equations were parametrized). Therefore, they could not investigate global structures, in particular, composed of different types of flows. In addition, accretion flows are generally thought to be transonic around the black hole. However, the local solution can deviate from the transonic solution, in particular, in the inner region where most of the X-ray is emitted.

In this paper, we consider global structures of optically thin, two-temperature, black hole accretion disks incorporating magnetic fields. The main purpose is to account for the bright/hard state during the bright hard-to-soft transition. In particular, we focus on the transition from the low/hard state to the bright/hard state which can be explained by the transition from the ADAF/RIAF to the low- β disk. The basic equations are described in section 2. In section 3 and section 4, we present results of the global solutions. Section 5 is devoted to discussion. We summarize the paper in section 6.

2. Model and Assumptions

2.1. Basic Equations

In this section, we derive the basic equations for vertically integrated, one-dimensional steady-state, optically thin, two-temperature black hole accretion flows (e.g., Kato et al. 2008) incorporating magnetic fields (see also Oda et al. 2010) from the resistive MHD equations. We adopt cylindrical coordinates (ϖ, φ, z) . General relativistic effects are simulated using the pseudo-Newtonian potential $\psi = -GM/(r - r_s)$ (Paczynski & Wiita 1980), where G is the gravitational constant, M is the black hole mass (we assume $M = 10M_\odot$ in this paper), $r = (\varpi^2 + z^2)^{1/2}$, and $r_s = 2GM/c^2 \sim 2.95 \times 10^6 (M/10M_\odot)$ cm

is the Schwarzschild radius. For simplicity, the gas is assumed to consist of protons (ions) and electrons. The number density of ions and electrons are equal due to charge neutrality, $n = n_i = n_e$.

The resistive MHD equations are

$$\frac{\partial \rho}{\partial t} + \nabla \cdot (\rho \mathbf{v}) = 0, \quad (1)$$

$$\rho \left[\frac{\partial \mathbf{v}}{\partial t} + (\mathbf{v} \cdot \nabla) \mathbf{v} \right] = -\rho \nabla \psi - \nabla p_{\text{gas}} + \frac{\mathbf{j} \times \mathbf{B}}{c}, \quad (2)$$

$$\begin{aligned} \frac{\partial(\rho_e \epsilon_e)}{\partial t} + \nabla \cdot [(\rho_e \epsilon_e + p_e) \mathbf{v}] - (\mathbf{v} \cdot \nabla) p_e \\ = \delta_{\text{heat}} q^+ + q^{\text{ie}} - q_{\text{rad}}^-, \end{aligned} \quad (3)$$

$$\begin{aligned} \frac{\partial(\rho_i \epsilon_i)}{\partial t} + \nabla \cdot [(\rho_i \epsilon_i + p_i) \mathbf{v}] - (\mathbf{v} \cdot \nabla) p_i \\ = (1 - \delta_{\text{heat}}) q^+ - q^{\text{ie}}, \end{aligned} \quad (4)$$

$$\frac{\partial \mathbf{B}}{\partial t} = \nabla \times \left(\mathbf{v} \times \mathbf{B} - \frac{4\pi}{c} \eta_{\text{m}} \mathbf{j} \right), \quad (5)$$

where $\rho = \rho_i + \rho_e$ is the density, $\rho_i = m_i n$ and $\rho_e = m_e n$ are the ion and electron densities, m_i and m_e are the ion and electron masses, \mathbf{v} is the velocity, \mathbf{B} is the magnetic field, $\mathbf{j} = c \nabla \times \mathbf{B} / 4\pi$ is the current density, $p_{\text{gas}} = p_i + p_e = nk(T_i + T_e)$ is the gas pressure, p_i and p_e are the ion and electron gas pressure, T_i and T_e are the ion and electron temperature, k is the Boltzmann constant, $\epsilon_i = (p_i / \rho_i) / (\gamma_i - 1)$ and $\epsilon_e = (p_e / \rho_e) / (\gamma_e - 1)$ are the internal energy of ions and electrons. Here, $\gamma_i = 5/3$ and $\gamma_e = \gamma_e(T_e)$ are the specific-heat ratio for ions and electrons (details in section 2.4). In the energy equations for electrons (3) and ions (4), q^+ is the heating rate, q_{rad}^- is the radiative cooling rate, and q^{ie} is the energy transfer rate from ions to electrons via Coulomb collisions. Here, δ_{heat} represents the fraction of heating to electrons. In this paper, we assume that δ_{heat} is constant for simplicity. In the induction equation (5), $\eta_{\text{m}} \equiv c^2 / 4\pi \sigma_c$ is the magnetic diffusivity, where σ_c is the electric conductivity.

2.1.1. Azimuthally Averaged Equations

Three-dimensional global and local MHD simulations of black hole accretion disks showed that magnetic fields inside the disk are turbulent and dominated by the azimuthal component both in the ADAF/RIAF-like state and in the low- β disk state (e.g., Machida et al. 2006; Johansen & Levin 2008). On the basis of results of the simulations, we decompose the magnetic fields into the mean fields, $\bar{\mathbf{B}} = (0, \bar{B}_\varphi, 0)$, and fluctuating fields, $\delta \mathbf{B} = (\delta B_\varpi, \delta B_\varphi, \delta B_z)$, and also decomposed the velocity into the mean velocity, $\bar{\mathbf{v}} = (v_\varpi, v_\varphi, v_z)$, and the fluctuating velocity, $\delta \mathbf{v} = (\delta v_\varpi, \delta v_\varphi, \delta v_z)$. We assume that the fluctuating components vanish when azimuthally averaged, $\langle \delta \mathbf{v} \rangle = \langle \delta \mathbf{B} \rangle = 0$, and that the radial and vertical components of the magnetic fields are negligible compared with the azimuthal component, $|\bar{B}_\varphi + \delta B_\varphi| \gg |\delta B_\varpi|, |\delta B_z|$ (see the left panel in figure 2). Here, $\langle \rangle$ denotes the azimuthal average.

We assume that the disk is in a steady state and in hydrostatic balance in the vertical direction. By azimuthally averaging equations (1) - (5) and ignoring the second order terms of $\delta \mathbf{v}$, δB_φ , and δB_z , we obtain

$$\frac{1}{\varpi} \frac{\partial}{\partial \varpi} (\varpi \rho v_\varpi) + \frac{\partial}{\partial z} (\rho v_z) = 0, \quad (6)$$

$$\rho v_\varpi \frac{\partial v_\varpi}{\partial \varpi} + \rho v_z \frac{\partial v_\varpi}{\partial z} - \frac{\rho v_\varpi^2}{\varpi} = -\rho \frac{\partial \psi}{\partial \varpi} - \frac{\partial p_{\text{tot}}}{\partial \varpi} - \frac{\langle B_\varphi^2 \rangle}{4\pi \varpi}, \quad (7)$$

$$\begin{aligned} \rho v_\varpi \frac{\partial v_\varphi}{\partial \varpi} + \rho v_z \frac{\partial v_\varphi}{\partial z} + \frac{\rho v_\varpi v_\varphi}{\varpi} \\ = \frac{1}{\varpi^2} \frac{\partial}{\partial \varpi} \left[\varpi^2 \frac{\langle B_\varphi B_\varphi \rangle}{4\pi} \right] + \frac{\partial}{\partial z} \left(\frac{\langle B_\varphi B_z \rangle}{4\pi} \right) \end{aligned} \quad (8)$$

$$0 = -\frac{\partial \psi}{\partial z} - \frac{1}{\rho} \frac{\partial p_{\text{tot}}}{\partial z}, \quad (9)$$

$$\begin{aligned} \frac{\partial}{\partial \varpi} [(\rho_e \epsilon_e + p_e) v_\varpi] + \frac{v_\varpi}{\varpi} (\rho_e \epsilon_e + p_e) + \frac{\partial}{\partial z} [(\rho_e \epsilon_e + p_e) v_z] \\ - v_\varpi \frac{\partial}{\partial \varpi} p_e - v_z \frac{\partial}{\partial z} p_e = \delta_{\text{heat}} q^+ + q^{\text{ie}} - q_{\text{rad}}^-, \end{aligned} \quad (10)$$

$$\begin{aligned} \frac{\partial}{\partial \varpi} [(\rho_i \epsilon_i + p_i) v_\varpi] + \frac{v_\varpi}{\varpi} (\rho_i \epsilon_i + p_i) + \frac{\partial}{\partial z} [(\rho_i \epsilon_i + p_i) v_z] \\ - v_\varpi \frac{\partial}{\partial \varpi} p_i - v_z \frac{\partial}{\partial z} p_i = (1 - \delta_{\text{heat}}) q^+ - q^{\text{ie}}, \end{aligned} \quad (11)$$

$$\begin{aligned} 0 = -\frac{\partial}{\partial z} [v_z \langle B_\varphi \rangle] - \frac{\partial}{\partial \varpi} [v_\varpi \langle B_\varphi \rangle] + \{ \nabla \times \langle \delta \mathbf{v} \times \delta \mathbf{B} \rangle \}_\varphi \\ - \{ \eta_m \nabla \times (\nabla \times \bar{\mathbf{B}}) \}_\varphi, \end{aligned} \quad (12)$$

where $p_{\text{tot}} = p_{\text{gas}} + p_{\text{mag}}$ is the total pressure and $p_{\text{mag}} = \langle B_\varphi^2 \rangle / 8\pi$ is the azimuthally averaged magnetic pressure. The last term on the right-hand side of equation (7) represents the magnetic tension force. The third and fourth terms on the right-hand side of equation (12) represent the dynamo term and the magnetic diffusion term. We approximate the induction equation later, based on the results of the numerical simulations.

2.1.2. Vertically Integrated, Azimuthally Averaged Equations

We assume that the radial velocity, v_ϖ , the specific angular momentum, $\ell = \varpi v_\varphi$, and the plasma β ($\equiv p_{\text{gas}}/p_{\text{mag}}$) are independent of z , and that the disks are isothermal in the vertical direction for simplicity. The surface density, Σ , the vertically integrated total pressure, W_{tot} , and the half thickness of the disk, H , are defined as

$$\Sigma \equiv \int_{-\infty}^{\infty} \rho dz = \int_{-\infty}^{\infty} \rho_0 \exp \left(-\frac{1}{2} \frac{z^2}{H^2} \right) dz = \sqrt{2\pi} \rho_0 H, \quad (13)$$

$$\begin{aligned} W_{\text{tot}} \equiv \int_{-\infty}^{\infty} p_{\text{tot}} dz = \int_{-\infty}^{\infty} p_{\text{tot}0} \exp \left(-\frac{1}{2} \frac{z^2}{H^2} \right) dz \\ = \sqrt{2\pi} p_{\text{tot}0} H, \end{aligned} \quad (14)$$

$$\Omega_{\text{K}0}^2 H^2 = \frac{W_{\text{tot}}}{\Sigma}, \quad (15)$$

where $\Omega_{\text{K}0} = (GM/\varpi)^{1/2}/(\varpi - r_s)$ is the Keplerian angular velocity. Here, the subscript 0 refers to quantities in the equatorial plane. Using the equation of state for the ideal gas, the vertically integrated total pressure is expressed as

$$W_{\text{tot}} = W_{\text{gas}} + W_{\text{mag}} = \frac{kT_i + kT_e}{m_i + m_e} \Sigma (1 + \beta^{-1}). \quad (16)$$

The vertically integrated magnetic tension force is expressed as

$$\begin{aligned} \int_{-\infty}^{\infty} \frac{\langle B_\varphi^2 \rangle}{4\pi \varpi} dz &= \frac{1}{\varpi} \frac{2\beta^{-1}}{1 + \beta^{-1}} \int_{-\infty}^{\infty} p_{\text{tot}} dz \\ &= \frac{1}{\varpi} \frac{2\beta^{-1}}{1 + \beta^{-1}} W_{\text{tot}}. \end{aligned} \quad (17)$$

Now we integrate the other basic equations in the vertical direction. We obtain

$$\dot{M} = -2\pi \varpi \Sigma v_\varpi, \quad (18)$$

$$\begin{aligned} v_\varpi^2 \frac{\partial \ln(-v_\varpi)}{\partial \ln \varpi} + \frac{W_{\text{tot}}}{\Sigma} \frac{\partial \ln W_{\text{tot}}}{\partial \ln \varpi} \\ = \frac{\ell^2 - \ell_{\text{K}0}^2}{\varpi^2} - \frac{W_{\text{tot}}}{\Sigma} \frac{d \ln \Omega_{\text{K}0}}{d \ln \varpi} - \frac{2\beta^{-1}}{1 + \beta^{-1}} \frac{W_{\text{tot}}}{\Sigma}, \end{aligned} \quad (19)$$

$$\dot{M}(\ell - \ell_{\text{in}}) = -2\pi \varpi^2 \int_{-\infty}^{\infty} \frac{\langle B_\varphi B_\varphi \rangle}{4\pi} dz, \quad (20)$$

$$\begin{aligned} \frac{\dot{M}}{2\pi \varpi^2} \frac{kT_e}{m_i + m_e} \left[-a_e(T_e) \left(1 + \frac{d \ln a_e(T_e)}{d \ln T_e} \right) \frac{\partial \ln T_e}{\partial \ln \varpi} \right. \\ \left. + \frac{\partial \ln \Sigma}{\partial \ln \varpi} - \frac{\partial \ln H}{\partial \ln \varpi} \right] = \delta_{\text{heat}} Q^+ + Q^{\text{ie}} - Q_{\text{rad}}^-, \end{aligned} \quad (21)$$

$$\begin{aligned} \frac{\dot{M}}{2\pi \varpi^2} \frac{kT_i}{m_i + m_e} \left[-a_i \frac{\partial \ln T_i}{\partial \ln \varpi} + \frac{\partial \ln \Sigma}{\partial \ln \varpi} - \frac{\partial \ln H}{\partial \ln \varpi} \right] \\ = (1 - \delta_{\text{heat}}) Q^+ - Q^{\text{ie}}, \end{aligned} \quad (22)$$

$$\begin{aligned} \dot{\Phi} \equiv \int_{-\infty}^{\infty} v_\varpi \langle B_\varphi \rangle dz \\ = \int_{\varpi}^{\varpi_{\text{out}}} \int_{-\infty}^{\infty} [\{ \nabla \times \langle \delta \mathbf{v} \times \delta \mathbf{B} \rangle \}_\varphi \\ - \{ \eta_m \nabla \times (\nabla \times \bar{\mathbf{B}}) \}_\varphi] d\varpi dz + \text{const.}, \end{aligned} \quad (23)$$

where \dot{M} is the mass accretion rate (for simplicity, we ignore the radial dependence of the mass accretion rate), $\ell_{\text{K}0} = \varpi^2 \Omega_{\text{K}0}$ is the Keplerian angular momentum and ℓ_{in} is the specific angular momentum swallowed by the black hole. The second term on the right-hand side of equation (19) is a correction resulting from the fact that the radial component of the gravitational force changes with height (Matsumoto et al. 1984; Kato et al. 2008). This correction is not negligible compared to the pressure gradient force in general, and to the effective centrifugal force unless $H/\varpi \ll 1$. We can see this by rewriting this term in the form $-(\ell_{\text{K}0}^2/\varpi^2)(H/\varpi)^2(d \ln \Omega_{\text{K}0}/d \ln \varpi)$ using equation (15). In the energy equations, Q^+ , Q_{rad}^- , and Q^{ie} are

the vertically integrated heating rate, radiative cooling rate, and energy transfer rate from ions to electrons via Coulomb collisions, and $a_e(T_e) = 1/[\gamma_e(T_e) - 1]$ and $a_i = 1/(\gamma_i - 1)$. In equation (23), $\dot{\Phi}$ is the radial advection rate of the azimuthal magnetic flux (hereafter we call it the magnetic flux advection rate).

We combine the basic equations as,

$$\frac{\partial \ln(-v_\varpi)}{\partial \ln \varpi} = \frac{N_1}{D}, \quad \frac{\partial \ln T_e}{\partial \ln \varpi} = \frac{N_2}{D}, \quad \frac{\partial \ln T_i}{\partial \ln \varpi} = \frac{N_3}{D}, \quad (24)$$

where D , N_1 , N_2 , and N_3 are the functions of ϖ , v_ϖ , T_e , and T_i (details in appendix 1).

We integrate these equations from the outer boundary using the backward Euler method with the Newton-Raphson method (appendix 2). We substitute the Runge-Kutta method for the backward Euler method only when we fail to solve these equations using the backward Euler method. We adjust the parameter ℓ_{in} so that flows satisfy the regularity condition, $D = N_1 = N_2 = N_3 = 0$, at the radius of the critical point (so-called the shooting method). Specifically, we regard solutions as satisfying the regularity condition when the signs of D , N_1 , N_2 , and N_3 change around the radius of the critical point and D , N_1 , N_2 , and N_3 smoothly increase or decrease with decreasing the radius.

2.2. α -Prescription of the Maxwell Stress Tensor

Global MHD simulations of radiatively inefficient, accretion flows (e.g., Hawley & Krolik 2001; Machida et al. 2006) showed that the ratio of the azimuthally averaged Maxwell stress to the sum of the azimuthally averaged gas pressure and magnetic pressure is nearly constant ($\alpha_B \equiv -\langle B_\varpi B_\varphi / 4\pi \rangle / \langle p_{\text{gas}} + p_{\text{mag}} \rangle \sim 0.05 - 0.1$), except in the innermost plunging region near to the black hole. Global and local Radiation-MHD simulations of optically thick accretion flows also showed such relations between the Maxwell stress and the total pressure (e.g., Hirose et al. 2006; Ohsuga et al. 2009). On the basis of the simulation results, we assume that the azimuthally averaged $\varpi\varphi$ -component of the Maxwell stress inside the disk is proportional to the total (gas and magnetic) pressure,

$$\frac{\langle B_\varpi B_\varphi \rangle}{4\pi} = -\alpha p_{\text{tot}}. \quad (25)$$

Integrating in the vertical direction, we obtain

$$\int_{-\infty}^{\infty} \frac{\langle B_\varpi B_\varphi \rangle}{4\pi} dz = -\alpha W_{\text{tot}}. \quad (26)$$

This is one of the key assumptions in this paper. When the magnetic pressure is high, the stress can be high, even though the gas pressure is low. We can rewrite this relation in terms of the kinematic viscosity, ν , as

$$\nu = A_\nu \alpha \sqrt{c_{s0}^2 + c_{A0}^2} H, \quad (27)$$

where

$$A_\nu \equiv -\left(\frac{\Omega}{\Omega_{K0}} \frac{\partial \ln \Omega}{\partial \ln \varpi}\right)^{-1}, \quad (28)$$

$c_{s0} = \sqrt{p_{\text{gas}0}/\rho_0}$ is the sound speed, $c_{A0} = \sqrt{2p_{\text{mag}0}/\rho_0}$ is the Alfvén speed, and Ω is the angular velocity. We can roughly estimate $\nu \sim v_{\text{turb}} \times l_{\text{turb}}$ for turbulent viscosity, where v_{turb} and $l_{\text{turb}} (\sim H)$ are the characteristic velocity and scale length of turbulence, respectively. It can be generally expected that $v_{\text{turb}} \sim c_{s0}$ in the gas-pressure dominant case while $v_{\text{turb}} \sim c_{A0}$ in the magnetic pressure dominant case. Therefore, our formulation ($v_{\text{turb}} \sim \sqrt{c_{s0}^2 + c_{A0}^2}$) is reasonable.

2.3. Prescription of the Magnetic Flux Advection Rate

We complete the set of basic equations by prescribing the radial distribution of the magnetic flux advection rate on the basis of the result of global three-dimensional MHD simulations. Performing the integration in the second term of the induction equation (23), we obtain

$$\begin{aligned} \dot{\Phi} &\equiv \int_{-\infty}^{\infty} v_\varpi \langle B_\varphi \rangle dz = -v_\varpi B_0(\varpi) \sqrt{4\pi} H \\ &= [\text{dynamo and diffusion terms}] + \text{const.} \end{aligned} \quad (29)$$

where

$$B_0(\varpi) = \sqrt{8\pi} \left(\frac{kT_i + kT_e}{m_i + m_e} \right)^{1/2} \left(\frac{\Sigma}{\sqrt{2\pi}H} \right)^{1/2} \beta^{-1/2} \quad (30)$$

is the mean azimuthal magnetic field in the equatorial plane.

According to the result of the global three-dimensional MHD simulation by Machida et al. (2006), the magnetic flux advection rate at each radius is roughly unchanged from before and after the transition from the ADAF/RIAF-like disk to the low- β disk. Following this result, we adopt the magnetic flux advection rate as the parameter in order to complete the set of the basic equations. We then need to prescribe the radial dependence of the magnetic flux advection rate. The magnetic flux advection rate depends on various mechanisms, such as the escape of magnetic fluxes due to the magnetic buoyancy, the regeneration of azimuthal magnetic fields by the shear motion, the generation of magnetic turbulence through the MRI, dissipation of magnetic fields due to the magnetic diffusivity, and magnetic reconnection. If the sum of the dynamo term and the magnetic diffusion term is zero in the whole region, the magnetic flux advection rate is spatially uniform. The global three-dimensional MHD simulation performed by Machida et al. (2006) indicated that the magnetic advection rate increases with decreasing radius, specifically, $\dot{\Phi} \propto \varpi^{-1}$, in the quasi steady state as a result of magnetic dynamo and diffusivity processes. In this paper, we parametrize the radial dependence of $\dot{\Phi}$ by introducing a parameter ζ as follows:

$$\dot{\Phi} = \dot{\Phi}_{\text{out}} \left(\frac{\varpi}{\varpi_{\text{out}}} \right)^{-\zeta}, \quad (31)$$

where $\dot{\Phi}_{\text{out}}$ is the magnetic flux advection rate at the outer boundary $\varpi = \varpi_{\text{out}}$ and a function of α , \dot{M} , $\ell_{\text{out}} - \ell_{\text{in}}$, $T_{\text{out}} (= T_{e,\text{out}} + T_{i,\text{out}})$, and β_{out} (we illustrated the concept of the magnetic flux advection in the right panel in figure 2). The magnetic flux advection rate is spatially uniform

in the case that $\zeta = 0$, and increases with decreasing radius in the case that $\zeta > 0$. In this way, we prescribe the magnetic flux advection rate at a radius by setting $\dot{\Phi}_{\text{out}}$ and ζ . To avoid numerical difficulties concerning the choice of ℓ_{in} , we set $\ell_{\text{out}} - \ell_{\text{in}} = 0.5\ell_{\text{K0}}$, $T_{\text{out}} = 0.375T_{\text{vir}}$, and $\beta_{\text{out}} = 3$ so that $\dot{\Phi}_{\text{out}}$ has the unique value for given α and \dot{M} .

Equation (31) is the second key assumption in this paper. Prescribing the magnetic flux advection rate enables the magnetic pressure to increase when the disk temperature decreases. In contrast, if we prescribe the plasma β at each radius instead of the magnetic flux advection rate, a decrease in temperature results in a decrease in magnetic pressure. This is inconsistent with the results of three-dimensional MHD simulations (e.g., Machida et al. 2006).

2.4. Energy Equations

In the conventional theory, the viscous heating was expressed as $q_{\text{vis}}^+ = t_{\varpi\varphi}\varpi(d\Omega/d\varpi)$, where $t_{\varpi\varphi}$ is the $\varpi\varphi$ -component of the total stress. Three-dimensional MHD simulations of accretion disks indicated that the dissipation of turbulent magnetic field energy dominates the total dissipative heating rate throughout the disk, and is expressed as $q^+ \sim \langle B_{\varpi}B_{\varphi}/4\pi \rangle \varpi(d\Omega/d\varpi)$ (e.g., Hirose et al. 2006; Machida et al. 2006; Krolik et al. 2007: Hereafter, we refer to it as the magnetic heating rate). We employ magnetic heating as the heating mechanism inside the disk. Following these simulation results and using the α -prescription of the Maxwell stress tensor, equation (25), we set the vertically integrated heating rate as follows:

$$Q^+ = \int_{-\infty}^{\infty} \left[\frac{\langle B_{\varpi}B_{\varphi} \rangle}{4\pi} \Omega \frac{\partial \ln \Omega}{\partial \ln \varpi} \right] dz = -\alpha W_{\text{tot}} \Omega \frac{\partial \ln \Omega}{\partial \ln \varpi} . \quad (32)$$

We assume that the energy transfer from ions to electrons occurs via Coulomb collisions and use the energy transfer rate Q^{ie} given by Stepney and Guilbert (1983) and Dermer et al. (1991). We consider bremsstrahlung (Svensson 1982; Stepney & Guilbert 1983; Narayan & Yi 1995), synchrotron (Pacholczyk 1970; Mahadevan et al. 1996; Esin et al. 1996), and Compton cooling by bremsstrahlung and synchrotron photons (Dermer et al. 1991; Narayan & Yi 1995) as cooling processes [see Oda et al. (2010) for details]. The vertically integrated radiative cooling rate is expressed as

$$Q_{\text{rad}}^- = Q_{\text{br}}^- + Q_{\text{sy}}^- + Q_{\text{br,C}}^- + Q_{\text{sy,C}}^- . \quad (33)$$

On the left-hand side of the energy equations,

$$a_e(T_e) = \frac{1}{\gamma_e(T_e) - 1} = \frac{1}{\theta_e} \left[\frac{3K_3(1/\theta_e) + K_1(1/\theta_e)}{K_4(1/\theta_e)} - 1 \right] , \quad (34)$$

$$a_i = \frac{1}{(\gamma_i - 1)} = \frac{3}{2} , \quad (35)$$

where K_n are modified Bessel function of the second kind of the order n , $\theta_e \equiv kT_e/(m_e c^2)$ is the dimensionless electron temperature. The coefficient $a_e(T_e)$ varies from 3/2

in the case of a non-relativistic electrons to 3 in the case of a relativistic electrons (e.g., Chandrasekhar 1939; Esin et al. 1997). We assumed that $a_i = 3/2$ in the case of a non-relativistic ions because the thermal energy of ions never exceeds 10% of the ion rest mass energy in our solutions.

2.5. Outer Boundary Condition

We imposed the outer boundary condition at $\varpi_{\text{out}} = 1000r_s$,

$$\ell_{\text{out}} - \ell_{\text{in}} = 0.5\ell_{\text{K0}}(\varpi = \varpi_{\text{out}}) , \quad (36)$$

$$\left. \frac{\partial f_{\text{ad,e}}}{\partial \varpi} \right|_{\varpi=\varpi_{\text{out}}} = 0 , \quad (37)$$

and

$$\left. \frac{\partial f_{\text{ad,i}}}{\partial \varpi} \right|_{\varpi=\varpi_{\text{out}}} = 0 , \quad (38)$$

where $f_{\text{ad,e}}$ and $f_{\text{ad,i}}$ are the fraction of the heat advection to the heating for electrons and ions (so-called advection factors) defined as

$$f_{\text{ad,e}} \equiv \frac{Q_{\text{ad,e}}}{\delta_{\text{heat}} Q^+ + Q^{\text{ie}}} , \quad (39)$$

$$f_{\text{ad,i}} \equiv \frac{Q_{\text{ad,i}}}{(1 - \delta_{\text{heat}}) Q^+} , \quad (40)$$

respectively. Again, to avoid numerical difficulties concerning a choice of ℓ_{in} , we fixed $\ell_{\text{in}} = \ell_{\text{K0}}(\varpi = 3r_s)$ when we compute the outer boundary condition so that the outer boundary condition is unique for given α and \dot{M} .

Under the boundary condition, we obtain an ADAF/RIAF-type solution near the outer boundary for a low-mass accretion rate and a low- β disk-type boundary solution for a high-mass accretion rate. In the middle range of the mass-accretion rates, we obtain several types of boundary solutions, specifically, an ADAF/RIAF-type, SLE-type, LHAF-type, low- β disk-type, and/or intermediate-type solutions. In this case, we choose the boundary solution having the highest value of the advection factor for ions, that is, the boundary solution closest to the ADAF/RIAF-type one.

3. Global Solutions

We obtained global solutions of optically thin, two-temperature black hole accretion disks by numerically integrating the basic equations from the outer boundary. The free parameters were \dot{M} , α , δ_{heat} , and ζ .

We chose $\alpha = 0.05$ as an example of a pressure-gradient-driven flow and $\alpha = 0.2$ as an example of a viscosity-driven flow around the radius of the critical point (Matsumoto et al. 1984; Narayan et al. 1997; Nakamura et al. 1997). Also, the former corresponds to the case of a low transition luminosity from the ADAF/RIAF to the low- β disk, and the latter corresponds to the case of a high transition luminosity, because the maximum luminosity for the ADAF/RIAF is $L \sim 0.4\alpha^2 L_{\text{Edd}}$.

We chose $\zeta = 0.90$ as the fiducial value, so that the plasma β would be roughly uniform in ADAF/RIAF solutions (details in section 3.3). When ζ has a small value (e.g., $\zeta = 0$), we cannot obtain low- β disk solutions but usual ADAF/RIAF and LHAF solutions. In this case, the magnetic pressure becomes negligible compared to the gas pressure in the inner region. Hence, the equations reduce to that of the conventional model. On the other hand, when ζ is too large (e.g., $\zeta > 1$), the magnetic pressure always becomes dominant in the inner region, even at low mass-accretion rates.

The fraction of the magnetic heating δ_{heat} is a poorly constrained parameter. Yuan et al. (2003) suggested that $\delta_{\text{heat}} \sim 0.5$ be required to fit the spectrum of Sgr A* with the ADAF/RIAF model. Sharma et al. (2007) performed local shearing box simulations of the nonlinear evolution of the MRI in a collisionless plasma incorporating the pressure anisotropy, and showed that δ_{heat} is a function of T_e and T_i (approximately, $\delta_{\text{heat}} = \left[1 + 3\sqrt{T_i/T_e}\right]^{-1}$). However, we found no qualitative difference for any value of δ_{heat} in the low- β disk solutions (see also Oda et al. 2010). Even in the ADAF/RIAF solutions, we found small differences only in the electron temperature and advection factors in the inner region. Therefore, we choose $\delta_{\text{heat}} = 0.2$ as the fiducial value in this paper.

3.1. Radial Structure and Energy Balance of Global Solutions

First, we show the results for the case $\alpha = 0.05$, $\zeta = 0.9$, and $\delta_{\text{heat}} = 0.2$. Figure 3 shows the radial distribution of the electron temperature, T_e , the ion temperature, T_i , the plasma β , the magnetic field strength at the equatorial plane, B_0 , the radial velocity, v_ϖ , the surface density, Σ , the ratio of specific angular momentum to Keplerian angular momentum, ℓ/ℓ_{K0} , and the ratio of half thickness of the disk to radius, H/ϖ . We denote the radius of the critical point at which $D = N_1 = N_2 = N_3 = 0$ by the plus sign (+). The energy balance is illustrated in figure 4. The top and second panels show the radial distribution of the advection factors for ions $f_{\text{ad},i}$, and for electrons, $f_{\text{ad},e}$, respectively. In addition, we introduce the total advection factor,

$$f_{\text{ad}} \equiv \frac{Q_{\text{ad},e} + Q_{\text{ad},i}}{Q^+}, \quad (41)$$

in order to classify solutions; this is illustrated in the third panel. The bottom panel shows the radial distribution of the fraction of the magnetic heating rate to the total heating rate for electrons, $\delta_{\text{heat}}Q^+ / (\delta_{\text{heat}}Q^+ + Q^{\text{ie}})$, in order to illustrate which process mainly heats electrons, the magnetic heating or the energy transfer from ions. The disk parameters are summarized in table 1.

We describe five representative solutions with different mass-accretion rates. For an ADAF/RIAF solution ($f_{\text{ad}} \gtrsim 0.5$ in the entire region) when the mass accretion rate is low, $\dot{M}/\dot{M}_{\text{Edd}} = 1.089 \times 10^{-3}$ (gray dashed). For a critical ADAF/RIAF solution (the minimum value of $f_{\text{ad}} \sim 0$) when the mass accretion rate is close to the maximum

mass accretion rate for the ADAF/RIAF, $\dot{M}/\dot{M}_{\text{Edd}} = 8.043 \times 10^{-3}$ (gray thin solid). For a LHAF solution (the solution having the lowest negative value of f_{ad} , that is, the heat advection works as an effective heating most efficiently) when the mass accretion rate slightly exceeding the maximum mass accretion rate for the ADAF/RIAF, $\dot{M}/\dot{M}_{\text{Edd}} = 1.224 \times 10^{-2}$ (long dashed). For a low- β disk solution (the minimum value of $\beta \sim 0.1$) when the mass accretion rate is relatively high, $\dot{M}/\dot{M}_{\text{Edd}} = 2.246 \times 10^{-2}$ (short dashed). For an extremely low- β disk solution (the minimum value of $\beta \sim 0.01$) when the mass accretion rate is high, $\dot{M}/\dot{M}_{\text{Edd}} = 5.984 \times 10^{-2}$ (solid).

In the ADAF/RIAF solution, ions are heated by magnetic heating and a substantial fraction of the dissipated energy is advected inward. In the outer region, electrons are mainly heated by energy transfer from ions, and heat advection for electrons works as effective cooling. Meanwhile, electrons in the inner region are mainly heated by magnetic heating, and heat advection for electrons works as effective heating. A substantial fraction of the dissipated energy that heats electrons is radiated away.

In the critical ADAF/RIAF solution, the heat advection becomes inefficient around $60r_s$ where the energy transfer from ions to electrons via Coulomb collisions becomes efficient because the surface density increases. As a result, the ion temperature slightly decreases, and electrons receive almost all of the dissipated energy, which is radiated away around this radius.

In the LHAF solution, the radiative cooling becomes efficient in the middle region ($20r_s \lesssim \varpi \lesssim 100r_s$) because the surface density increases further. Therefore, the electron temperature decreases (but slightly). The ion temperature also decreases because ions are well coupled to electrons due to the efficient energy transfer via Coulomb collisions. Thus, the heat advection for both electrons and ions works as an effective heating in this transition layer from the high entropy region to the low entropy region. Such heat advection balances the radiative cooling.

In the low- β disk solution, the radiative cooling and the energy transfer from ions to electrons via Coulomb collisions become more efficient and overwhelm the heat advection except in the innermost plunging region ($\varpi \lesssim 4r_s$). The gas pressure decreases due to radiative cooling, while the magnetic pressure increases due to conservation of the magnetic flux advection rate at each radius. As a result, the total pressure still remains large. Therefore, the magnetic heating being proportional to the total pressure can be large enough to balance the radiative cooling.

In the extremely low- β disk solution, the structure of the disk is qualitatively the same as the low- β disk solution but the temperature is lower and the magnetic pressure becomes more dominant.

We also show the results for the case $\alpha = 0.2$, $\zeta = 0.9$, and $\delta_{\text{heat}} = 0.2$ in figure 5 and figure 6. We obtained solutions at mass accretion rates higher than the results for the case $\alpha = 0.05$ basically because the heating rate being proportional to α increases.

3.2. Force Balance in the Radial Direction

We describe force balance in the radial direction. The non-dimensional pressure gradient force, the effective centrifugal force, and the magnetic tension force are given by

$$f_p = -\frac{W_{\text{tot}}}{\Sigma} \frac{1}{\varpi} \frac{\partial \ln W_{\text{tot}}}{\partial \ln \varpi} \left(\frac{r_s}{c^2} \right), \quad (42)$$

$$f_c = \left[\frac{\ell^2 - \ell_{K0}^2}{\varpi^3} - \frac{W_{\text{tot}}}{\Sigma} \frac{1}{\varpi} \frac{d \ln \Omega_{K0}}{d \ln \varpi} \right] \left(\frac{r_s}{c^2} \right) \\ = \frac{\ell^2 - \ell_{K0}^2 \left[1 + \left(\frac{H}{\varpi} \right)^2 \frac{d \ln \Omega_{K0}}{d \ln \varpi} \right]}{\varpi^3} \left(\frac{r_s}{c^2} \right), \quad (43)$$

and,

$$f_m = -\frac{W_{\text{tot}}}{\Sigma} \frac{1}{\varpi} \frac{2\beta^{-1}}{1 + \beta^{-1}} \left(\frac{r_s}{c^2} \right), \quad (44)$$

which are derived from the second term on the left-hand side, the first and second terms, and the last term on the right-hand side of equation (19), respectively. We note that even in the case that $\ell = \ell_{K0}$, the centrifugal force has a non-zero (but trivial) value unless $H/\varpi \ll 1$ due to the presence of the correction factor for the gravitational force.

Figure 7 illustrates the radial distribution of the pressure gradient force (solid), the effective centrifugal force (dashed), and the magnetic tension force (dotted) in the inner region of the disks ($1.6r_s < \varpi < 10r_s$) for five representative solutions (the ADAF/RIAF, the critical ADAF/RIAF, the LHAF, the low- β disk, the extremely low- β disk from top to bottom) for the case $\alpha = 0.05$, $\zeta = 0.90$, and $\delta_{\text{heat}} = 0.2$. Just outside the radius of the critical point, the primary inward force is the effective centrifugal force when the mass accretion rate is low. As the mass accretion rate increases, the pressure gradient force becomes dominant, that is, the flow is pressure-gradient-driven. The nature of flows very near the radius of the critical point is the same as the conventional model (Nakamura et al. 1997; Narayan et al. 1997). However, this is not the case outside this region when the mass accretion rate is high; the magnetic tension force is the primary inward force. In other word, the pressure gradient force pushes the gas inward very near the radius of critical point, while the magnetic tension force pushes the disk gas inward outside this region.

Figure 8 illustrates the force balance for the case $\alpha = 0.20$, $\zeta = 0.90$, and $\delta_{\text{heat}} = 0.2$. In contrast to the results for the case $\alpha = 0.05$, the primary inward force is always the effective centrifugal force just outside the radius of the critical point; that is, the flow is viscosity-driven. However, as well as the results for the case $\alpha = 0.05$, the magnetic tension force is the primary inward force outside this region when the mass accretion rate is high.

3.3. Dependence on ζ

We investigated the dependence on the parameter ζ prescribing the radial dependence of the magnetic flux advection rate. We illustrate the radial distribution of the

plasma β and the magnetic field strength at the equatorial plane, B_0 , in figure 9, and the electron temperature and the ion temperature in figure 10. The disk parameters are $\alpha = 0.05$, $\delta_{\text{heat}} = 0.2$, $\zeta = 0.5$ (dashed), 0.75 (long dashed), 0.9 (solid), and 1 (dotted). The three representative solutions (ADAF/RIAF, LHAF, low- β disk solutions) are illustrated from the top panel to the bottom panel.

At low mass-accretion rates (i.e., the ADAF/RIAF solutions), the plasma β increases for $\zeta < 0.9$ and decreases for $\zeta > 0.9$ with decreasing radius, while being roughly uniform at ~ 5 for $\zeta = 0.9$. For this reason, we choose $\zeta = 0.9$ as the fiducial value in this paper.

In the ADAF/RIAF solution, the magnetic heating being proportional to the total pressure is insensitive to the magnetic pressure because the gas pressure dominates the total pressure. In addition, the radiative cooling that is contributed by the magnetic field via the synchrotron and synchrotron-Compton cooling are inefficient. Therefore, the electron and ion temperatures are roughly independent of ζ , while the plasma β and B_0 strongly depend on ζ .

As the mass accretion rate increases and exceeds the maximum mass accretion rate for the ADAF/RIAF (i.e., in the LHAF solutions), the radiative cooling becomes efficient in the middle region ($20r_s \lesssim \varpi \lesssim 100r_s$). For a lower magnetic flux advection rate (i.e., a smaller value of ζ), a larger decrease in gas pressure is required in order for the magnetic pressure to become high enough to support the disk. Therefore, the electron temperature and the ion temperature decrease more drastically in the transition layer ($\varpi \sim 25r_s$).

As the mass-accretion rate increases further, the transition layer retreats outward and the disk becomes cooler and more magnetic pressure dominant. We note that a lower magnetic flux advection rate (i.e., a smaller value of ζ) results in lower temperatures and lower plasma β in the inner region. In contrast, the magnetic field strength attains roughly the same level for different values of ζ .

4. Relations between \dot{M} , L versus Local Quantities

The relations between the mass-accretion rate (or the luminosity) and the physical quantities, such as the surface density, electron temperature at a radius, are widely used to understand the X-ray spectral state transition observed in BHCs. In this section, we consider these relations obtained from the global solutions.

Figure 11 shows the relations between Σ versus \dot{M} , T_e , T_i , and β at $\varpi = 5r_s$ for the case $\alpha = 0.05$, $\delta_{\text{heat}} = 0.2$, $\zeta = 0.90$ (black), 0.75 (gray), and 0.50 (open diamond). We obtained ADAF/RIAF branches in the low mass-accretion rate and high-temperature region, and low- β disk branches in the high mass-accretion rate and low-temperature region.

Not the mass-accretion rate, but the luminosity is an observable quantity. The electron temperature and the Compton y parameter are fundamental parameters of X-ray spectral fitting with the thermal Comptonization

model. To make it easier to compare our results with observations, we also show the relation between T_e and the Compton y parameter at $\varpi = 5r_s$ versus L in figure 12. We calculated the luminosity L by integrating the radiative cooling rate over $1.6r_s < \varpi < 500r_s$ for a given mass-accretion rate. Note that the most luminous region is not the inner boundary, but the region around the radius of the critical point where the surface density is high. The Compton y parameter is given by

$$y \equiv \frac{4kT_e}{m_e c^2} \left(1 + \frac{4kT_e}{m_e c^2} \right) \tau_{es} (1 + \tau_{es}) . \quad (45)$$

When the luminosity is very low ($L \lesssim 10^{-5} L_{\text{Edd}}$), both the energy transfer from ions to electrons and the radiative cooling are extremely inefficient, because the surface density is very low. Thus heat advection is dominant for not only ions, but also electrons, $Q_{\text{ad},i} \sim (1 - \delta_{\text{heat}})Q^+$ and $Q_{\text{ad},e} \sim \delta_{\text{heat}}Q^+$. The electron and ion temperatures are determined mainly by these energy equations. Since the heat-advection terms and the magnetic-heating term have the same dependence on the mass accretion rate, the electron and ion temperatures are independent of the mass accretion rate (hence the luminosity), and are roughly the virial temperatures, respectively.

When the luminosity is below and close to the maximum luminosity for the ADAF/RIAF ($10^{-5} L_{\text{Edd}} \lesssim L \lesssim 0.4\alpha^2 L_{\text{Edd}} \sim 0.001 L_{\text{Edd}}$), the radiative cooling becomes efficient for electrons, $Q_{\text{ad},e} + Q_{\text{rad}}^- \sim \delta_{\text{heat}}Q^+$, because the surface density is relatively high. However, the heat advection still remains dominant for ions, $Q_{\text{ad},i} \sim (1 - \delta_{\text{heat}})Q^+$. As a result, the electron temperature weakly anti-correlates with the luminosity, while the ion temperature still remains constant.

When the luminosity exceeds the maximum luminosity for the ADAF/RIAF ($L \gtrsim 0.001 L_{\text{Edd}}$), the radiative cooling and the energy transfer from ions to electrons become dominant, $Q_{\text{rad}}^- \sim \delta_{\text{heat}}Q^+ + Q^{\text{ie}}$ and $Q^{\text{ie}} \sim (1 - \delta_{\text{heat}})Q^+$. Hence, electrons receive a substantial fraction of the magnetic heating, and the radiative cooling balances the magnetic heating, $Q_{\text{rad}}^- \sim Q^+$. In other words, electrons and ions are strongly coupled via Coulomb collisions, and the flow is radiatively efficient. As a result, the electron temperature strongly anti-correlates with the luminosity.

When the luminosity is high, the Compton y parameter correlates with the luminosity for $\zeta = 0.9$ and 0.75 , and anti-correlates with the luminosity for $\zeta = 0.5$.

We show these relations for the case $\alpha = 0.2$ in figure 13 and figure 14. In this case, the maximum mass accretion rate and the luminosity for the ADAF/RIAF increases ($\dot{M}_{\text{c,A}} \sim 0.05 \dot{M}_{\text{Edd}}$ and $L_{\text{c,A}} \sim 0.016 L_{\text{Edd}}$). The luminosity in the low- β disk branch exceeds $\sim 0.1 L_{\text{Edd}}$. The Compton y parameter correlates with the luminosity for all cases because the electron temperature is relatively high and gently decreases with the luminosity compared to the results for the case $\alpha = 0.05$.

5. Discussion

First, we briefly remark why we can obtain low- β disk solutions. In our model, a decrease in the gas pressure results in an increase in the magnetic pressure because due to the conservation of the magnetic flux advection rate at a certain radius. Therefore, even if an efficient radiative cooling decreases the gas pressure, the magnetic pressure can increase and support the disk in the vertical direction. In addition, the magnetic heating being proportional to the total pressure can balance such an efficient radiative cooling. In this way, we can obtain low- β disk solutions.

We also remark that such low- β disks are essentially different from MDAFs in terms of the energy balance and the configuration of magnetic fields. The MDAFs appear in the innermost plunging region of optically thin accretion disks in global MHD and general relativistic MHD simulations (e.g., Fragile & Meier 2009). Outside the innermost plunging region, the magnetic fields become turbulent because the growth timescale of the MRI is shorter than the inflow timescale. The generation of magnetic turbulence owing to the MRI balances the dissipation, and the dissipated energy is converted into thermal energy efficiently. In such flows, the magnetic heating rate is consistent with the prediction of the α -prescription of the stress tensor, that is, proportional to the total pressure. This heating balances the heat advection in the ADAF/RIAF and the radiative cooling in the low- β disk. In addition, the magnetic fields are dominated by the azimuthal component because the timescale of the stretching of the magnetic fields owing to the shear motion is also shorter than the inflow timescale. On the other hand, in the innermost plunging region, the ratio of the time scales is reversed, because the inflow velocity increases with decreasing the radius and exceeds the Alfvén velocity. Therefore, the magnetic field lines are stretched out in the radial direction before the MRI grows, and generates turbulence. Since there is no turbulence, no dissipation occurs. As a result, a substantial fraction of the gravitational energy is converted into the radial infall kinetic energy without being converted into thermal energy. In such flows, the magnetic heating rate predicted by the α -prescription can no longer be valid, and there is almost no heating. Hence, the gas pressure and temperature become low, and the flow becomes magnetically-dominated. To sum up, in the low- β disk, the magnetic fields are turbulent and dominated by the azimuthal component, and the magnetic heating balances the radiative cooling. However, in the MDAF very close to the black hole, the magnetic fields are coherent and dominated by the radial component, and there is no magnetic heating. Although both the low- β disk and the MDAF are cool and magnetically-dominated, they are essentially different.

5.1. Transition from ADAF/RIAF to Low- β Disk through LHAF

In this subsection, we describe how the ADAF/RIAF undergoes a transition to the low- β disk as the mass accretion rate increases. The transition is illustrated schemat-

ically in figure 15.

When the mass-accretion rate is below the maximum mass-accretion rate for the ADAF/RIAF, we obtained the ADAF/RIAF solutions that are essentially the same as the solutions of the conventional model (bottom panel in figure 15).

At the mass-accretion rate slightly exceeding the maximum mass accretion rate for the ADAF/RIAF, the radiative cooling overwhelms the heat advection, working as effective cooling in the middle region ($\varpi \sim 50r_s$). The gas pressure decreases due to the radiative cooling while the magnetic pressure increases because of the conservation of magnetic flux advection rates given at a radius. In this way, the magnetic pressure becomes dominant and supports the disk in this region, and the flow undergoes a transition from the outer ADAF/RIAF to the low- β disk. The LHAF appears in this narrow transition layer from the outer ADAF/RIAF to the low- β disk because such a flow configuration results in the negative entropy gradient. In the inner region ($\varpi \lesssim 10r_s$), the radiative cooling is still inefficient because the surface density decreases and the radial velocity steeply increases with decreasing the radius (such a feature is more prominent for lower α ; see also Nakamura et al. 1997; Narayan et al. 1997). Therefore, the flow returns to the ADAF/RIAF. As a result, the flow is composed of the outer ADAF/RIAF, the LHAF inside the narrow transition layer, the low- β disk, and the inner ADAF/RIAF (third panel in figure 15).

We note that such an inner ADAF/RIAF cannot be obtained from self-similar solutions of optically thin disks. In the self-similar solutions, the radiative cooling can be efficient, even in the inner region because the surface density increases and the radial velocity gently increases with decreasing radius ($\Sigma \propto \varpi^{-1/2}$, $v_\varpi \propto \varpi^{-1/2}$). However, the self-similar solutions are no longer valid in the inner region because of the transonic nature of the flow.

As the mass-accretion rate increases further, the radiative cooling becomes more efficient over the whole region. Thus, the transition layer between the outer ADAF/RIAF and the low- β disk retreats, and the inner ADAF/RIAF region diminishes. In other words, the low- β region becomes wider. Eventually, the whole region becomes the low- β disk, except in the innermost ADAF/RIAF region around the radius of the critical point (first panel in figure 15).

5.2. Dynamical Property

Transonic flows around black holes with the α -prescription of the stress tensor are divided into two classes according to the value of α , a pressure-gradient-driven flow for small α and a viscous-driven flow for large α (e.g., Matsumoto et al. 1984; Nakamura et al. 1997; Narayan et al. 1997). We calculated the solution with $\alpha = 0.05$ as an example of the pressure-gradient-driven flow and the solution with $\alpha = 0.2$ as an example of the viscous-driven flow.

First, we discuss the case for $\alpha = 0.05$. When the mass-accretion rate is around or above the maximum mass-accretion rate for the ADAF/RIAF, the surface density

decreases and the radial velocity increases sharply with decreasing the radius in the inner region ($\varpi \lesssim 10r_s$). Just outside the radius of the critical point, the angular momentum of the flow approaches and exceeds the Keplerian angular momentum. In this region, the primary inward force is the pressure gradient force.

Next, we discuss the case for $\alpha = 0.2$. In this case, the radial distribution of the surface density is relatively flat compared to the case for $\alpha = 0.05$ and the angular momentum is always below the Keplerian angular momentum. Just outside the radius of the critical point, the primal inward force is the effective centrifugal force; that is, the gas falls inward due to losses of its angular momentum.

Our solutions have essentially the same nature of transonic flows just outside the radius of the critical point as the conventional model. In addition to this nature, we found that the primal inward force is the magnetic tension force at some distance from the radius of the critical point; that is, the magnetic tension pushes the disk gas more strongly than the other forces in this region. This is a new finding of our results. The magnetic field can contribute to not only the vertical hydrostatic balance, but also the radial force balance in some part of the disk.

5.3. Application to Bright/Hard State during Bright Hard-to-Soft Transition

The relations between Σ versus \dot{M} , T_e , T_i , and β are consistent with the thermal equilibrium solutions presented by Oda et al. (2010). We note that the LHAF branches do not appear at such an inner region, because the transition layer from the outer ADAF/RIAF to the low- β disk appears in the middle region ($\varpi \sim 50r_s$) first, and retreats as the mass accretion rate increases.

We calculated the luminosity by integrating the radiative cooling rate over $1.6r_s < \varpi < 500r_s$. When the luminosity is very low ($L \lesssim 10^{-5}L_{\text{Edd}}$ for $\alpha = 0.05$ and $L \lesssim 10^{-4}L_{\text{Edd}}$ for $\alpha = 0.2$), the electron temperature is roughly independent of the luminosity and $\sim 10^{10.3}\text{K}$. This indicates that the cutoff energy in the X-ray spectrum is independent of the luminosity (the clear cutoff at such a low luminosity, however, may not be detectable).

When the luminosity is below the maximum luminosity for the ADAF/RIAF, ($L \lesssim 0.001L_{\text{Edd}}$ for $\alpha = 0.05$ and $L \lesssim 0.016L_{\text{Edd}}$ for $\alpha = 0.2$), the electron temperature weakly anti-correlates with the luminosity in the range from $\sim 10^{9.5}\text{K}$ to $\sim 10^{10.3}\text{K}$. Note that the minimum electron temperature for the ADAF/RIAF is roughly independent of the value of α . This feature agrees with the result presented by Esin et al. (1998). This weak anti-correlation between the electron temperature and the luminosity in the high electron temperature region can be consistent with the weak anti-correlation between the energy cutoff and the luminosity observed in the low/hard state. However, the ADAF/RIAF cannot account for the electron temperature lower than $\sim 10^{9.5}\text{K}$.

When the luminosity is above the maximum luminosity for the ADAF/RIAF, the electron temperature strongly anti-correlates with the luminosity in the range from \sim

10^8K to $\sim 10^{9.5}\text{K}$. This strong anti-correlation in the relatively low electron temperature and high luminosity region can be consistent with the anti-correlation between the energy cutoff and the luminosity observed in the bright/hard state. Therefore, we conclude that the low- β disk can account for the bright/hard state, and that the transition from the ADAF/RIAF to the low- β disk corresponds to the transition from the low/hard state to the bright/hard state during the bright hard-to-soft transition.

We also touch on the possibility of the dark hard-to-soft transition during which the system immediately undergoes a transition from the low/hard state to the high/soft state at a low luminosity. When ζ has a small value, and thus, the magnetic flux advection rate is very low in the inner region, we could not obtain an optically thin global solution at a mass-accretion rate higher than the maximum mass accretion rate for the ADAF/RIAF. In this case, we expect that the ADAF/RIAF undergoes a transition to an optically thick disk (e.g., the standard disk, the slim disk, and an optically thick low- β disk) with the LHAF transition layer. This might correspond to the dark hard-to-soft transition.

5.4. What Mechanism Determines the Magnetic Flux Advection Rate?

We propose a possible scenario that what mechanism determines whether the system undergoes the bright hard-to-soft transition or the dark hard-to-soft transition. Three-dimensional MHD/Radiation-MHD simulations showed that the polarity of the azimuthal magnetic field inside the disk can change in time alternately in the ADAF/RIAF and the standard disk, that is, the gas pressure dominant disk (e.g., Nishikori et al. 2006; Shi et al. 2010). Large filament-like structures of magnetic fields emerge from the mid plane of the disk and rise up, roughly, in the growth timescale of the Parker instability. Subsequently, reversals of azimuthal magnetic fields take place in the mid plane, and the polarity of azimuthal magnetic fields alternates successively. (Note that such a change in polarity can be suppressed in the low- β disk because the growth timescale of the Parker instability is quite long). The pattern of the polarity is symmetrical with respect to the equatorial plane roughly, but not exactly. Hence, the magnetic flux advection rate inside the disk can change in time.

If the mass-accretion rate exceeds the threshold for the onset of the cooling instability when the magnetic flux advection rate is high on average, the ADAF/RIAF will evolve toward the low- β disk with the LHAF transition layer. In this case, we can expect that the system undergoes the bright hard-to-soft transition. On the other hand, if the mass accretion rate exceeds the threshold when the magnetic flux advection rate is low, the ADAF/RIAF will evolve toward an optically thick disk with the LHAF transition layer. In this case, we can expect the dark hard-to-soft transition.

5.5. Beyond the Low- β Disk: Episodic Ejections of Relativistic Jets

According to Pessah and Psaltis (2005), the MRI is stabilized for toroidal Alfvén speeds exceeding the geometrical mean of the sound speed and the rotational speed of the disk gas ($v_A \gtrsim \sqrt{c_s v_{K0}}$). In mildly low- β disk solutions at moderately high mass accretion rates, this condition is not satisfied, that is, the MRI is not stabilized. On the other hand, in extremely low- β disk solutions at very high-mass accretion rates, this condition is satisfied in a certain region, and thus, the MRI can be stabilized. Hence, we expect that no magnetic turbulence can be driven, and then no magnetic heating can occur in this region (although the amplification of azimuthal magnetic fields due to the shear motion may still survive). Therefore, the cooling instability will occur and the disk will shrink further in the vertical direction. As a result, the magnetic field strength and energy inside the disk can be amplified further. Such a drastic and further increase in the magnetic field energy may lead to an explosive energy release (e.g., Shibata et al. 1990; Yuan et al. 2009). The timing analyses on the X-ray spectrum and the radio emission of BHCs suggest that episodic ejections of relativistic jets take place during the transition from the bright/hard state to the soft state (e.g., Fender et al. 2009). This explosive energy release from the low- β disk may be an origin of the episodic ejections of relativistic jets.

6. Summary

We have calculated vertically integrated, one-dimensional, steady-state global solutions of optically thin, two-temperature, black hole accretion disks incorporating the mean azimuthal magnetic fields. We have obtained the magnetic pressure dominant (low- β) disk solutions at high mass-accretion rates. We have concluded that the low- β disk can account for the bright/hard state (or simply, the brightening of the hard state) observed during the bright hard-to-soft transition in transient outbursts of BHCs.

We have assumed that the $\varpi\varphi$ -component of the azimuthally averaged Maxwell stress tensor is proportional to the sum of the gas and magnetic pressure. We have also prescribed the radial distribution of the magnetic flux advection rate by introducing the parameter ζ in order to complete the set of basic equations. Accordingly, a decrease in temperature results in an increase in magnetic pressure under conservation of the magnetic flux advection rate at each radius, and the magnetic heating being proportional to the total pressure can balance the radiative cooling.

When the mass-accretion rate is below the maximum mass accretion rate for the ADAF/RIAF, we obtained the usual ADAF/RIAF solutions. When the mass accretion rate is just beyond the maximum mass accretion rate for the ADAF/RIAF, we obtained the solutions of the flow composed of the outer ADAF/RIAF, the LHAF inside the transition layer from the outer ADAF/RIAF to the low-

β disk, the low- β disk, and the inner ADAF/RIAF. This low- β disk region becomes wider as the mass-accretion rate increases further. Eventually, the whole region becomes the low- β disk, except in the innermost plunging region around the radius of the critical point. The electron temperature decreases from $\sim 10^{9.5}\text{K}$ to $\sim 10^8\text{K}$ with increasing the luminosity above the maximum luminosity for the ADAF/RIAF ($L \gtrsim 0.4\alpha^2 L_{\text{Edd}}$). This is consistent with the anti-correlation between the energy cutoff in the X-ray spectrum (hence the electron temperature) and the luminosity when $L \gtrsim 0.1L_{\text{Edd}}$, observed in the bright/hard state during the bright hard-to-soft transition of BHCs.

When we assumed very low magnetic flux advection rates, we could not obtain the low- β disk solutions. In this case, we expect that the flow will be composed of the outer ADAF/RIAF, the LHAF inside the transition layer from the outer ADAF/RIAF to an inner optically thick disk, and the inner optically thick disk at the maximum mass accretion rate for the ADAF/RIAF. This might correspond to the dark hard-to-soft transition.

Although we could obtain the extremely low- β disk solution at a very high mass accretion rate, the MRI can be stabilized in such an extremely low- β plasma. Hence, the magnetic heating due to turbulent magnetic fields may not occur under such an extremely low- β regime. In this case, the cooling instability will occur and the disk will shrink further in the vertical direction. As a result, the magnetic field energy can be amplified further. Such a drastic increase in magnetic field energy may lead to an explosive energy release. This can be an origin of the episodic ejections of relativistic jets observed during the bright hard-to-soft transition.

We would like to thank Feng Yuan for helpful discussions and comments. This work was supported in part by the Grant-in-Aid for Science Research of the Ministry of Education, Culture, Sports, Science and Technology (R.M.: 20340040), Grant-in-Aid for JSPS Fellows (20.1842), the Natural Science Foundation of China (grant 10833002, 10821302, 10825314, 1105110416, and 111330005), and the National Basic Research Program of China (973 Program 2009CB824800).

Appendix 1. Combined Form of Basic Equations

Combining the basic equations, we rewrite the set of the basic equations in the following form:

$$\mathbf{A} \cdot \mathbf{x} = \mathbf{b} , \quad (\text{A1})$$

$$\mathbf{A} = \begin{bmatrix} (1+\beta^{-1})\mu - \beta_{53} & \Gamma_e \beta_{03} & \Gamma_i \beta_{03} \\ \Delta_e \beta_{53} + \frac{3}{2} & A_e(T_e) - \Delta_e \Gamma_e \beta_{03} & -\Delta_e \Gamma_i \beta_{03} \\ \Delta_i \beta_{53} + \frac{3}{2} & -\Delta_i \Gamma_e \beta_{03} & a_i - \Delta_i \Gamma_i \beta_{03} \end{bmatrix} , \quad (\text{A2})$$

$$\mathbf{x} = \begin{bmatrix} \frac{\partial \ln(-v_\varpi)}{\partial \ln \varpi} \\ \frac{\partial \ln T_e}{\partial \ln \varpi} \\ \frac{\partial \ln T_i}{\partial \ln \varpi} \end{bmatrix} , \quad (\text{A3})$$

$$\mathbf{b} = \begin{bmatrix} \frac{u_{\text{K}0}}{\theta(1+\beta^{-1})} - \beta_{53} \frac{d \ln \Omega_{\text{K}0}}{d \ln \varpi} - \beta_{03} \beta^{-1} (1-2\zeta) + \frac{1-\beta^{-1}}{1+\beta^{-1}} \\ -\frac{\delta_{\text{heat}}}{\Gamma_e} \frac{u_{\text{in}}}{\theta} + \Delta_e \beta_{03} \beta^{-1} \left(\frac{d \ln \Omega_{\text{K}0}}{d \ln \varpi} + 1 - 2\zeta \right) + \frac{d \ln \Omega_{\text{K}0}}{d \ln \varpi} - 1 - S_e \\ -\frac{1-\delta_{\text{heat}}}{\Gamma_i} \frac{u_{\text{in}}}{\theta} + \Delta_i \beta_{03} \beta^{-1} \left(\frac{d \ln \Omega_{\text{K}0}}{d \ln \varpi} + 1 - 2\zeta \right) + \frac{d \ln \Omega_{\text{K}0}}{d \ln \varpi} - 1 - S_i \end{bmatrix} , \quad (\text{A4})$$

where

$$\begin{aligned} \mu &= \frac{(v_\varpi/c)^2}{(1+\beta^{-1})^2 \theta} , \quad \theta = \frac{kT_i + kT_e}{(m_i + m_e)c^2} , \quad \Gamma_i = \frac{T_i}{T_i + T_e} , \\ \Gamma_e &= \frac{T_e}{T_i + T_e} , \quad \beta_{53} \equiv \frac{2+5\beta^{-1}}{2+3\beta^{-1}} , \quad \beta_{03} \equiv \frac{2}{2+3\beta^{-1}} , \\ u_{\text{K}0} &\equiv \frac{\ell^2 - \ell_{\text{K}0}^2}{\varpi^2 c^2} , \quad u_{\text{in}} \equiv \frac{\ell^2 - \ell_{\text{in}}^2}{\varpi^2 c^2} , \\ \Delta_e &\equiv \frac{\delta_{\text{heat}}}{\Gamma_e} \frac{\alpha^2}{\mu} - \frac{1}{2} , \quad \Delta_i \equiv \frac{1 - \delta_{\text{heat}}}{\Gamma_i} \frac{\alpha^2}{\mu} - \frac{1}{2} , \\ S_e &\equiv \frac{2\pi\varpi^2}{\dot{M}} \frac{Q^{\text{ie}} - Q_{\text{rad}}^-}{kT_e/(m_i + m_e)} , \\ S_i &\equiv -\frac{2\pi\varpi^2}{\dot{M}} \frac{Q^{\text{ie}}}{kT_i/(m_i + m_e)} , \\ A_e(T_e) &= a_e(T_e) \left(1 + \frac{d \ln a_e(T_e)}{d \ln T_e} \right) . \end{aligned}$$

We define the denominator and the numerators in equation (24) as

$$D \equiv \det \mathbf{A} , \quad \begin{bmatrix} N_1 \\ N_2 \\ N_3 \end{bmatrix} \equiv \text{adj} \mathbf{A} \cdot \mathbf{b} , \quad (\text{A5})$$

where $\text{adj} \mathbf{A}$ is the adjugate matrix of \mathbf{A} .

Appendix 2. Integration Method

Introducing $\mathbf{X} = [\ln v_\varpi, \ln T_e, \ln T_i]$, $R = \ln \varpi$, and $\mathbf{F} = [N_1/D, N_2/D, N_3/D]$, we rewrite equation (24) in the following form:

$$\frac{\partial \mathbf{X}}{\partial R} = \mathbf{F}(R, \mathbf{X}) . \quad (\text{A6})$$

The difference equation in backward Euler method is given by

$$\frac{\mathbf{X}_{i+1} - \mathbf{X}_i}{\Delta R_i} = \mathbf{F}(R_{i+1}, \mathbf{X}_{i+1}) , \quad (\text{A7})$$

where $\Delta R_i \equiv R_{i+1} - R_i$. Here we define the residual ϕ as

$$\phi(\mathbf{X}_{i+1}) \equiv \mathbf{X}_{i+1} - \mathbf{X}_i - \Delta R_i \mathbf{F}(R_{i+1}, \mathbf{X}_{i+1}) . \quad (\text{A8})$$

We solve $\phi = 0$ using Newton-Raphson method. Let \mathbf{X}_{i+1}^n be the current approximation. Then the next approximation \mathbf{X}_{i+1}^{n+1} is given by

$$\mathbf{X}_{i+1}^{n+1} = \mathbf{X}_{i+1}^n - [\phi'(\mathbf{X}_{i+1}^n)]^{-1} \phi(\mathbf{X}_{i+1}^n). \quad (\text{A9})$$

Here ϕ' denotes the derivative ϕ with respect to \mathbf{X}_{i+1} .

References

- Abramowicz, M. A., Chen, X., Kato, S., Lasota, J.-P., & Regev, O. 1995, *ApJL*, 438, L37
- Balbus, S. A., & Hawley, J. F. 1991, *ApJ*, 376, 214
- Begelman, M. C., & Pringle, J. E. 2007, *MNRAS*, 375, 1070
- Belloni, T., et al. 2006, *MNRAS*, 367, 1113
- Bu, D.-F., Yuan, F., & Xie, F.-G. 2009, *MNRAS*, 392, 325
- Chandrasekhar, S. 1939, *An Introduction to the Study of Stellar Structure* (Chicago: Univ. Chicago Press)
- Dermer, C. D., Liang, E. P., & Canfield, E. 1991, *ApJ*, 369, 410
- Eardley, D. M., Lightman, A. P., & Shapiro, S. L. 1975, *ApJL*, 199, L153
- Esin, A. A., Narayan, R., Ostriker, E., & Yi, I. 1996, *ApJ*, 465, 312
- Esin, A. A., McClintock, J. E., & Narayan, R. 1997, *ApJ*, 489, 865
- Esin, A. A., Narayan, R., Cui, W., Grove, J. E., & Zhang, S.-N. 1998, *ApJ*, 505, 854
- Fender, R. P., Homan, J., & Belloni, T. M. 2009, *MNRAS*, 396, 1370
- Fragile, P. C., & Meier, D. L. 2009, *ApJ*, 693, 771
- Gierliński, M., & Newton, J. 2006, *MNRAS*, 370, 837
- Hirose, S., Krolik, J. H., & Stone, J. M. 2006, *ApJ*, 640, 901
- Hawley, J. F., & Krolik, J. H. 2001, *ApJ*, 548, 348
- Homan, J., & Belloni, T. 2005, *Ap&SS*, 300, 107
- Ichimaru, S. 1977, *ApJ*, 214, 840
- Johansen, A., & Levin, Y. 2008, *A&A*, 490, 501
- Joinet, A., Kalemci, E., & Senziani, F. 2008, *ApJ*, 679, 655
- Kato, S., Fukue, J., & Mineshige, S. 2008, *Black-Hole Accretion Disks: Towards a New Paradigm* (Kyoto: Kyoto University Press)
- Krolik, J. H., Hirose, S., & Blaes, O. 2007, *ApJ*, 664, 1045
- Machida, M., Nakamura, K. E., & Matsumoto, R. 2006, *PASJ*, 58, 193
- Mahadevan, R., Narayan, R., & Yi, I. 1996, *ApJ*, 456, 327
- Matsumoto, R., Kato, S., Fukue, J., & Okazaki, A. T. 1984, *PASJ*, 36, 71
- Meier, D. L. 2005, *Ap&SS*, 300, 55
- Mineshige, S., Kusnosc, M., & Matsumoto, R. 1995, *ApJL*, 445, L43
- Miyakawa, T., Yamaoka, K., Homan, J., Saito, K., Dotani, T., Yoshida, A., & Inoue, H. 2008, *PASJ*, 60, 637
- Motta, S., Belloni, T., & Homan, J. 2009, *MNRAS*, 400, 1603
- Nakamura, K. E., Kusnosc, M., Matsumoto, R., & Kato, S. 1997, *PASJ*, 49, 503
- Narayan, R., Kato, S., & Honma, F. 1997, *ApJ*, 476, 49
- Narayan, R., & Yi, I. 1994, *ApJL*, 428, L13
- Narayan, R., & Yi, I. 1995, *ApJ*, 452, 710
- Nishikori, H., Machida, M., & Matsumoto, R., 2006, *ApJ*, 641, 862
- Oda, H., Machida, M., Nakamura, K. E., & Matsumoto, R. 2007, *PASJ*, 59, 457
- Oda, H., Machida, M., Nakamura, K. E., & Matsumoto, R. 2009, *ApJ*, 697, 16
- Oda, H., Machida, M., Nakamura, K. E., & Matsumoto, R. 2010, *ApJ*, 712, 639
- Ohsuga, K., Mineshige, S., Mori, M., & Kato, Y. 2009, *PASJ*, 61, L7
- Pacholczyk, A. G. 1970, *Radio Astrophysics* (San Fransico: Freeman)
- Paczynsky, B. & Wiita, P. J. 1980, *A&A*, 88, 23
- Pariev, V. I., Blackman, E. G., & Boldyrev, S. A. 2003, *A&A*, 407, 403
- Parker, E. N. 1966, *ApJ*, 145, 811
- Pessah, M. E., & Psaltis, D. 2005, *ApJ*, 628, 879
- Poutanen, J., & Svensson, R. 1996, *ApJ*, 470, 249
- Shakura, N. I., & Sunyaev, R. A. 1973, *A&A*, 24, 337
- Sharma, P., Quataert, E., Hammett, G. W., & Stone, J. M. 2007, *ApJ*, 667, 714
- Shapiro, S. L., Lightman, A. P., & Eardley, D. M. 1976, *ApJ*, 204, 187
- Shi, J., Krolik, J. H., & Hirose, S. 2010, *ApJ*, 708, 1716
- Shibata, K., Tajima, T., & Matsumoto, R. 1990, *ApJ*, 350, 295
- Shibazaki, N., & Hōshi, R. 1975, *Progress of Theoretical Physics*, 54, 706
- Stepney, S., & Guilbert, P. W. 1983, *MNRAS*, 204, 1269
- Sunyaev, R. A., & Titarchuk, L. G. 1980, *A&A*, 86, 121
- Svensson, R. 1982, *ApJ*, 258, 335
- Thorne, K. S., & Price, R. H. 1975, *ApJL*, 195, L101
- Titarchuk, L. 1994, *ApJ*, 434, 570
- Yuan, F. 2001, *MNRAS*, 324, 119
- Yuan, F. 2003, *ApJL*, 594, L99
- Yuan, F., Lin, J., Wu, K., & Ho, L. C. 2009, *MNRAS*, 395, 2183
- Yuan, F., Quataert, E., & Narayan, R. 2003, *ApJ*, 598, 301
- Yuan, F., & Zdziarski, A. A. 2004, *MNRAS*, 354, 953
- Yuan, F., Zdziarski, A. A., Xue, Y., & Wu, X.-B. 2007, *ApJ*, 659, 541

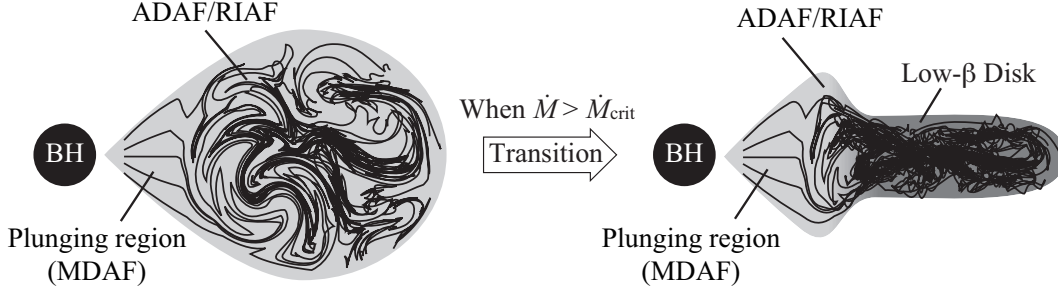


Fig. 1. Transition from an ADAF/RIAF-like disk to a low- β disk. The left panel illustrates the ADAF/RIAF-like disk state at a low mass accretion rate before the transition. The right panel illustrates the low- β disk state at a moderately high mass accretion rate after the transition. Solid curves depict magnetic field lines. In both states, the magnetic fields inside the accretion disk are turbulent and dominated by the azimuthal component except in the innermost plunging regions (the MDAF regions).

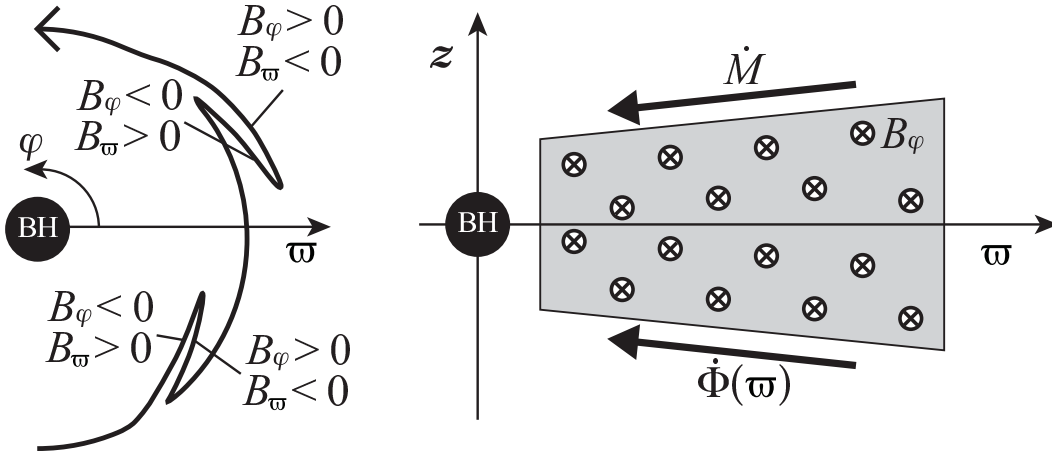


Fig. 2. Schematic pictures of magnetic field lines inside the accretion disk. Left: Structures of turbulent magnetic fields driven by the MRI. Right: Magnetic flux advection with mass accretion.

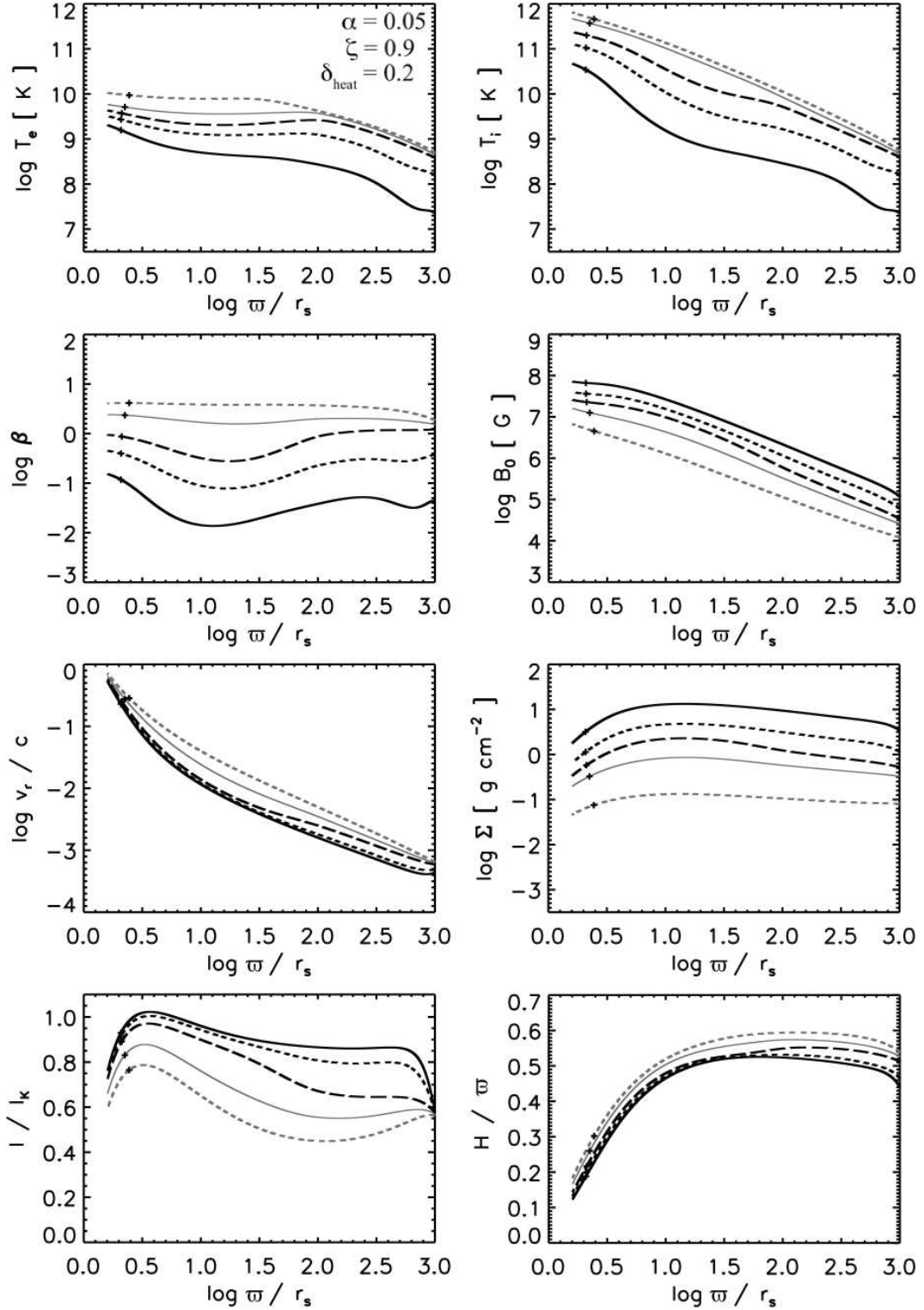


Fig. 3. Radial structures of optically thin, two-temperature accretion disks for the case $\dot{M}/\dot{M}_{\text{Edd}} = 2.089 \times 10^{-3}$ (gray dashed), 8.043×10^{-3} (gray thin solid), 1.224×10^{-2} (long dashed), 2.246×10^{-2} (short dashed), and 5.984×10^{-2} (solid), which correspond to the ADAF/RIAF, the critical ADAF/RIAF, the LHAF, the low- β disk, and the extremely low- β disk solutions, respectively. The disk parameters are $\alpha = 0.05$, $\zeta = 0.90$, and $\delta_{\text{heat}} = 0.2$. The radius of the critical point is denoted by the plus sign (+).

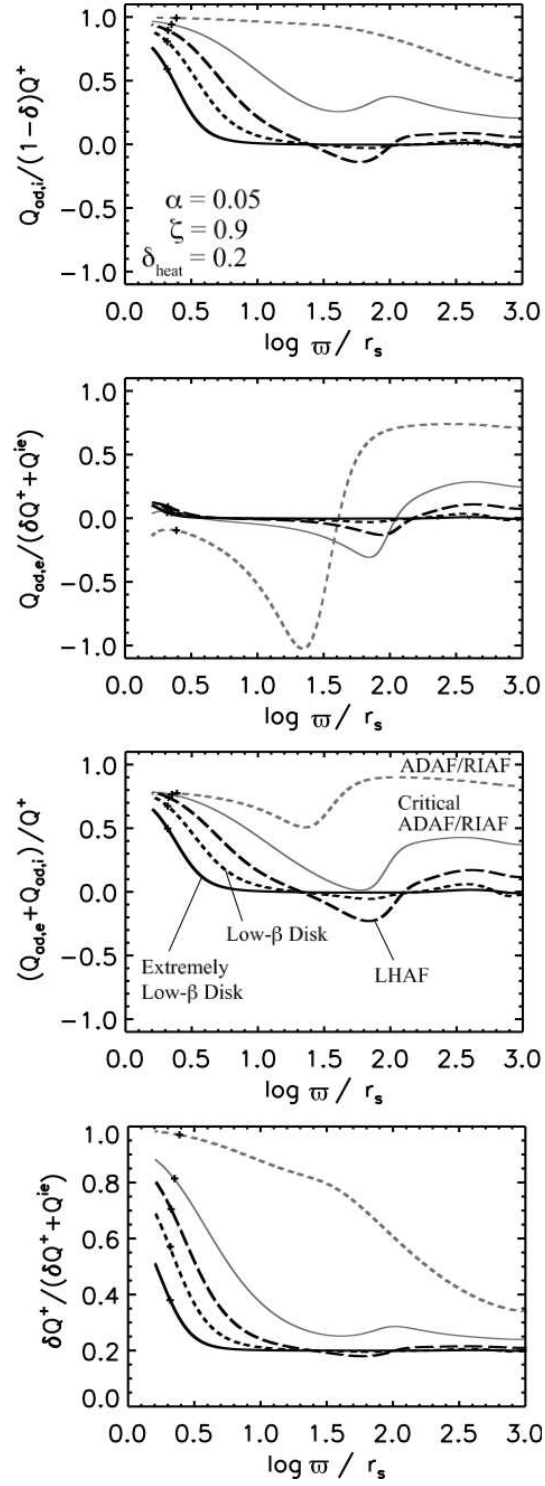


Fig. 4. Energy balance for the case $\alpha = 0.05$, $\zeta = 0.90$, and $\delta_{\text{heat}} = 0.2$. Top: the advection factor for ions. Second: the advection factor for electrons. Third: the total advection factor. Bottom: the fraction of the magnetic heating to the total heating rate for electrons.

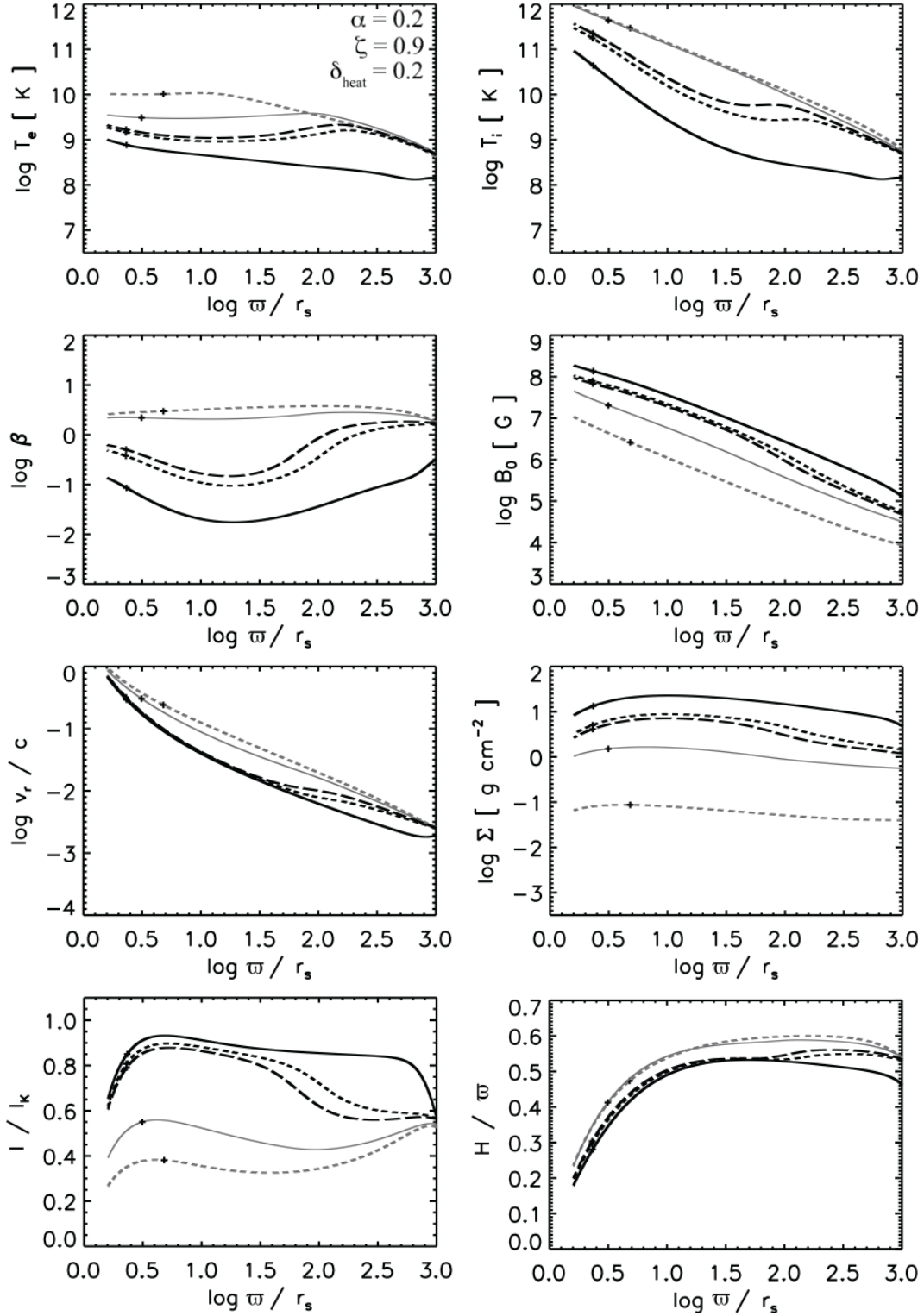


Fig. 5. Radial structures of optically thin, two-temperature accretion disks for the case $\dot{M}/\dot{M}_{\text{Edd}} = 3.993 \times 10^{-3}$ (gray dashed), 5.712×10^{-2} (gray thin solid), 1.202×10^{-1} (long dashed), 1.445×10^{-1} (short dashed), and 3.631×10^{-1} (solid), which correspond to the ADAF/RIAF, the critical ADAF/RIAF, the LHAF, the low- β disk, and the extremely low- β disk solutions, respectively. The disk parameters are $\alpha = 0.20$, $\zeta = 0.90$, and $\delta_{\text{heat}} = 0.2$.

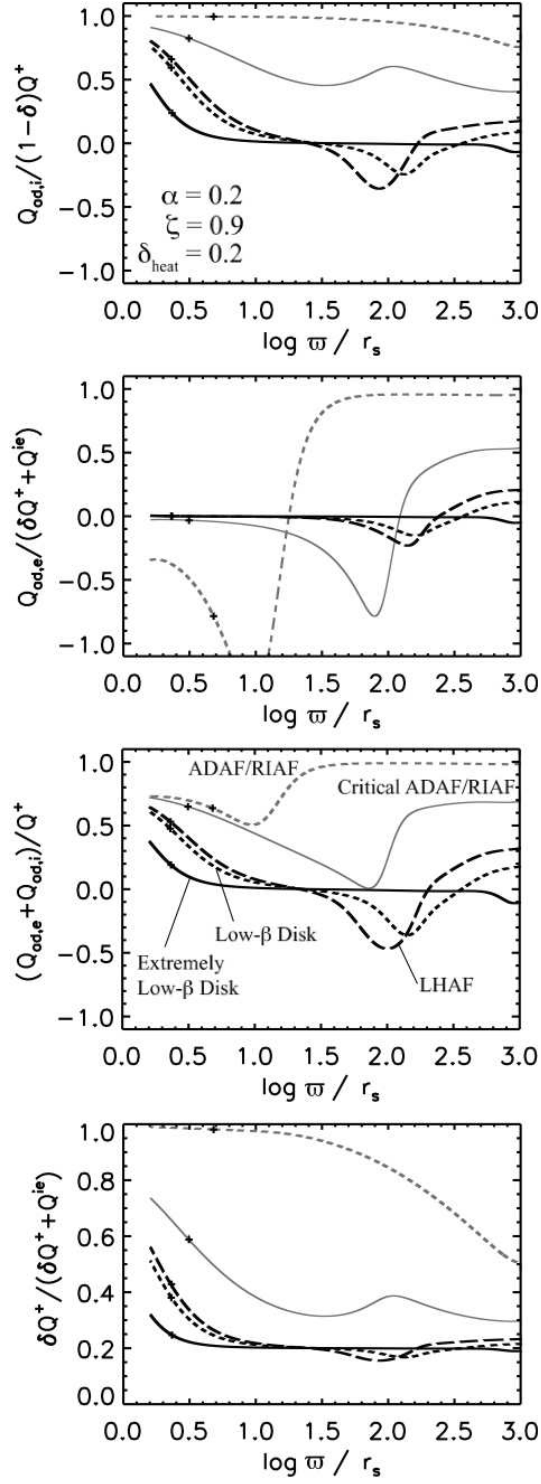


Fig. 6. Energy balance for the case $\alpha = 0.20$, $\zeta = 0.90$, and $\delta_{\text{heat}} = 0.2$.

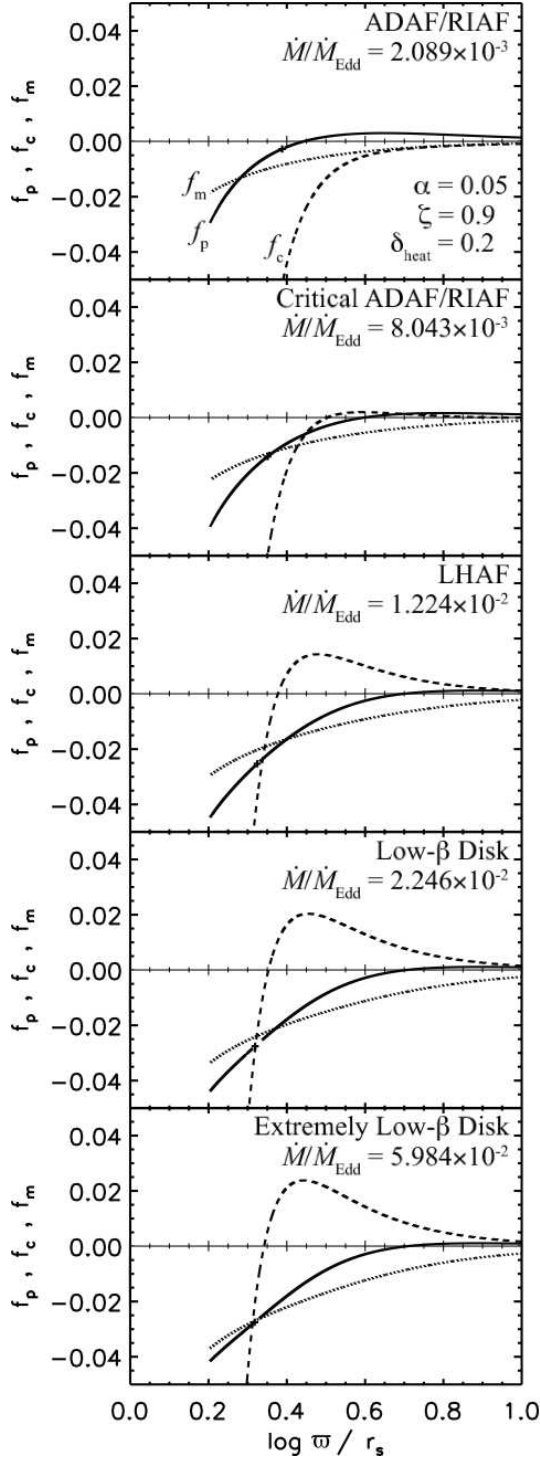


Fig. 7. Force balance in the radial direction for the case $\alpha = 0.05$, $\zeta = 0.90$, and $\delta_{\text{heat}} = 0.2$. From top to bottom, $\dot{M}/\dot{M}_{\text{Edd}} = 2.089 \times 10^{-3}$, 8.043×10^{-3} , 1.224×10^{-2} , 2.246×10^{-2} , and 5.984×10^{-2} . Pressure gradient force, f_p , (solid), effective centrifugal force, f_c , (dashed), and magnetic tension force f_m , (dotted).

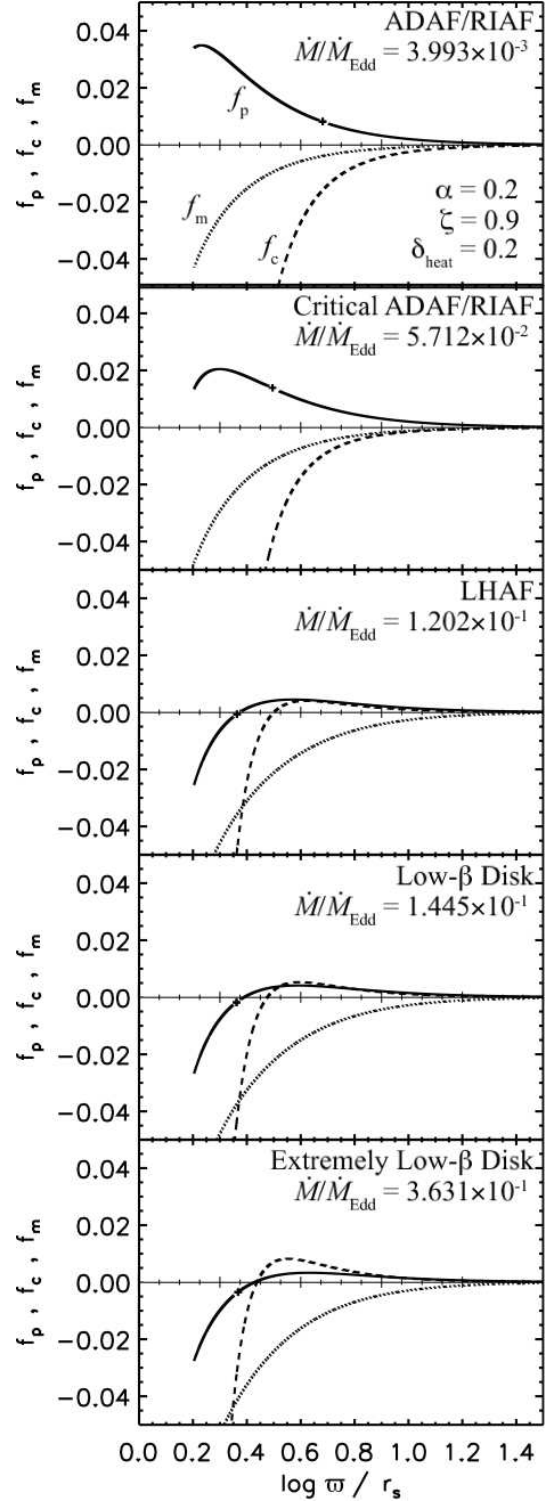


Fig. 8. Force balance in the radial direction for the case $\alpha = 0.20$, $\zeta = 0.90$, and $\delta_{\text{heat}} = 0.2$. From top to bottom, $\dot{M}/\dot{M}_{\text{Edd}} = 3.993 \times 10^{-3}$, 5.712×10^{-2} , 1.202×10^{-1} , 1.445×10^{-1} , and 3.631×10^{-1} . Pressure gradient force, f_p , (solid), effective centrifugal force, f_c , (dashed), and magnetic tension force f_m , (dotted).

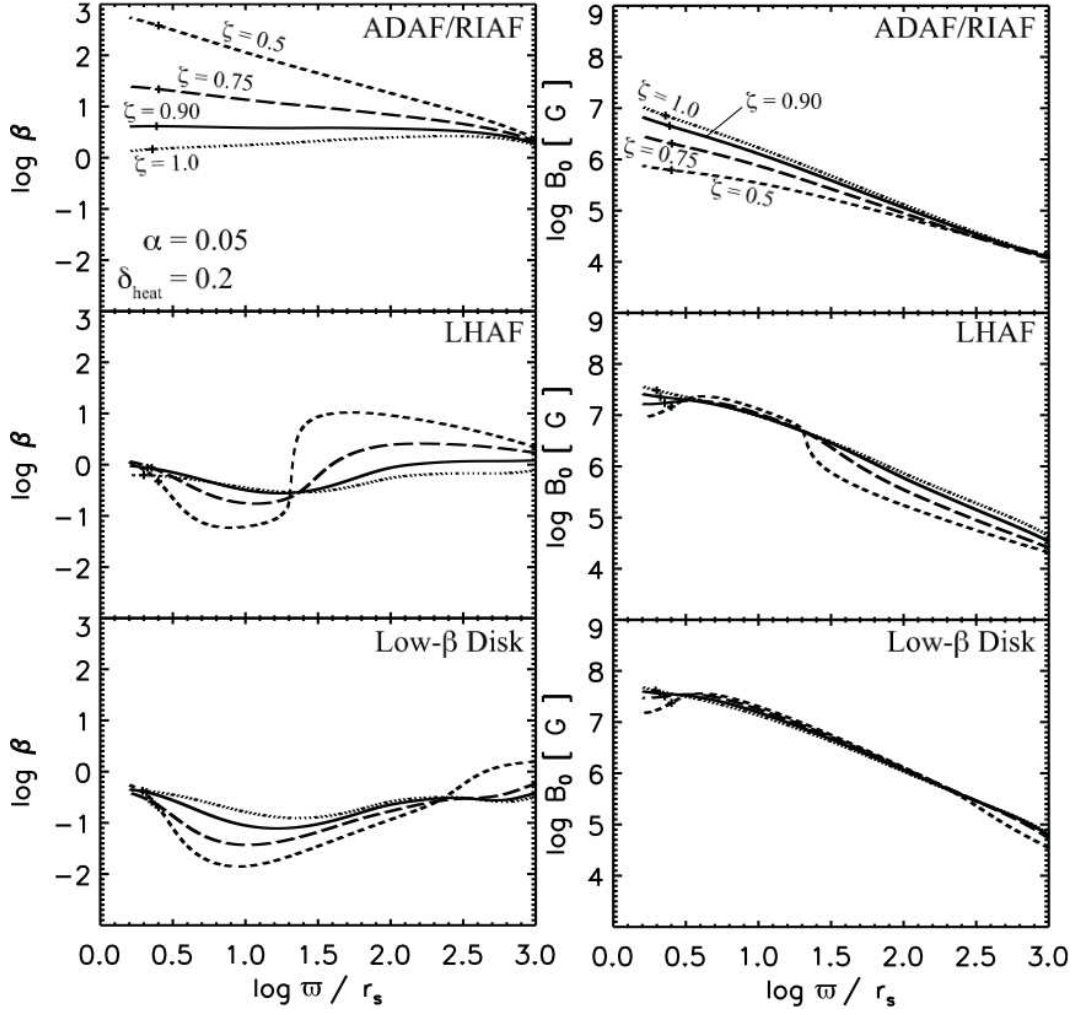


Fig. 9. Radial distribution of β (left) and B_0 (right). Three representative solutions (ADAF/RIAF, LHAF, and low- β disk) are illustrated from top to bottom. The disk parameters are $\alpha = 0.05$, $\delta_{\text{heat}} = 0.2$, $\zeta = 0.50$ (dashed), 0.75 (long dashed), 0.90 (solid), and 1.00 (dotted).

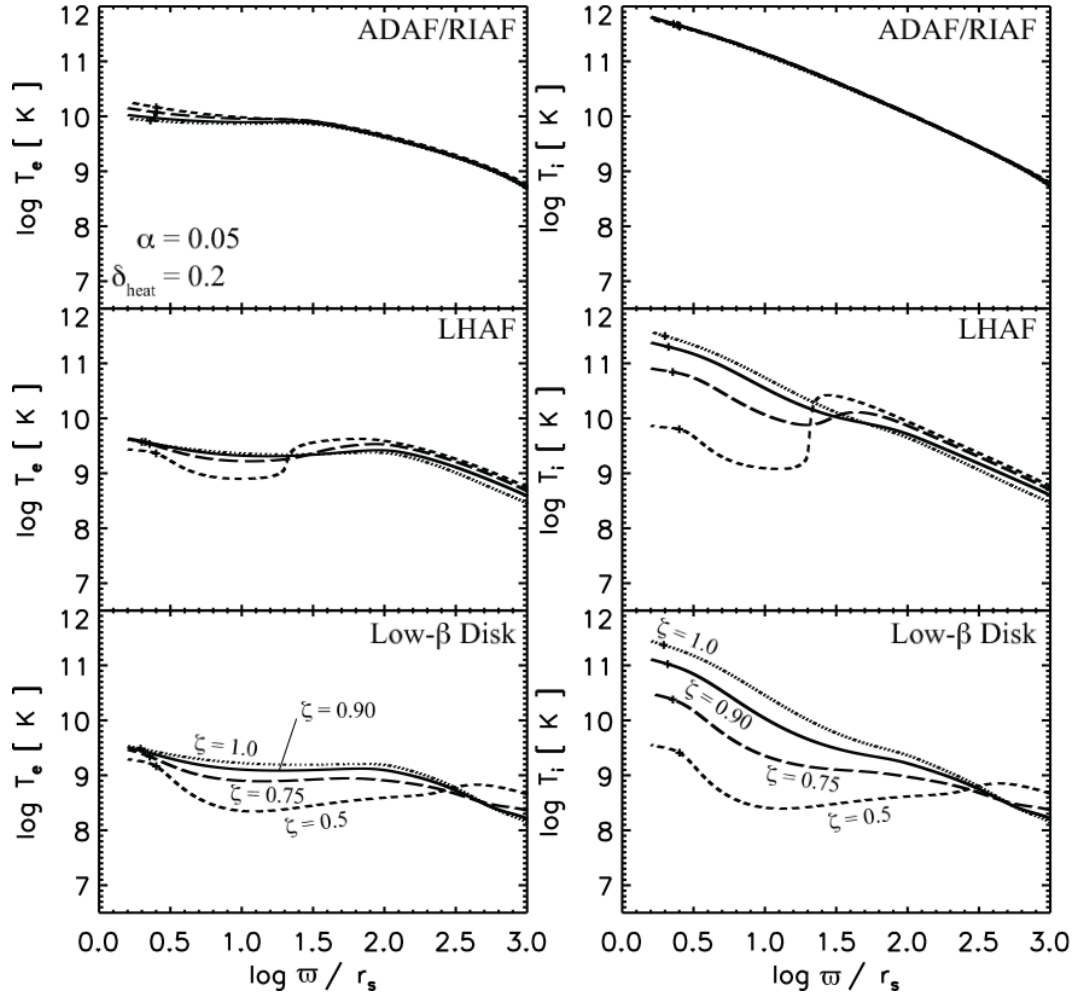


Fig. 10. Radial distribution of the electron temperature (left) and the ion temperature (right). Three representative solutions (ADAF/RIAF, LHAF, and low- β disk) are illustrated from top to bottom. The disk parameters are $\alpha = 0.05$, $\delta_{\text{heat}} = 0.2$, $\zeta = 0.50$ (dashed), 0.75 (long dashed), 0.90 (solid), and 1.00 (dotted).

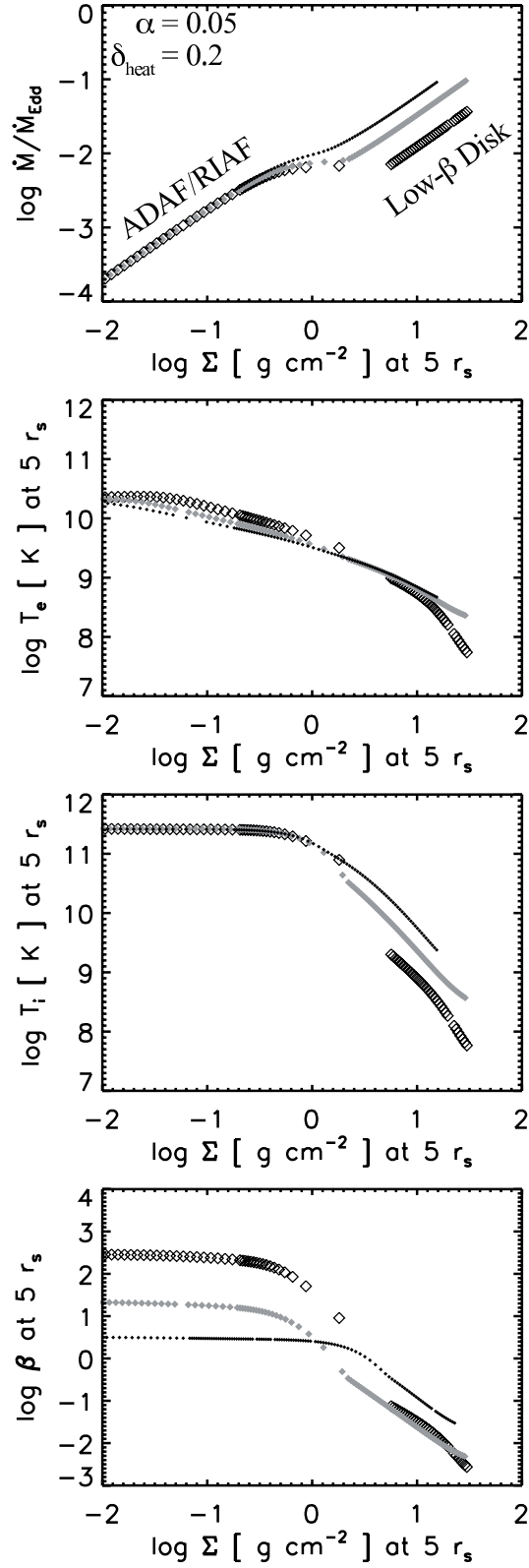


Fig. 11. Relation between Σ versus \dot{M} (top), T_e (second), T_i (third), and β (bottom) at $\varpi = 5r_s$. The disk parameters are $\alpha = 0.05$, $\delta_{\text{heat}} = 0.2$, $\zeta = 0.90$ (black), $\zeta = 0.75$ (gray), and $\zeta = 0.50$ (open diamond).

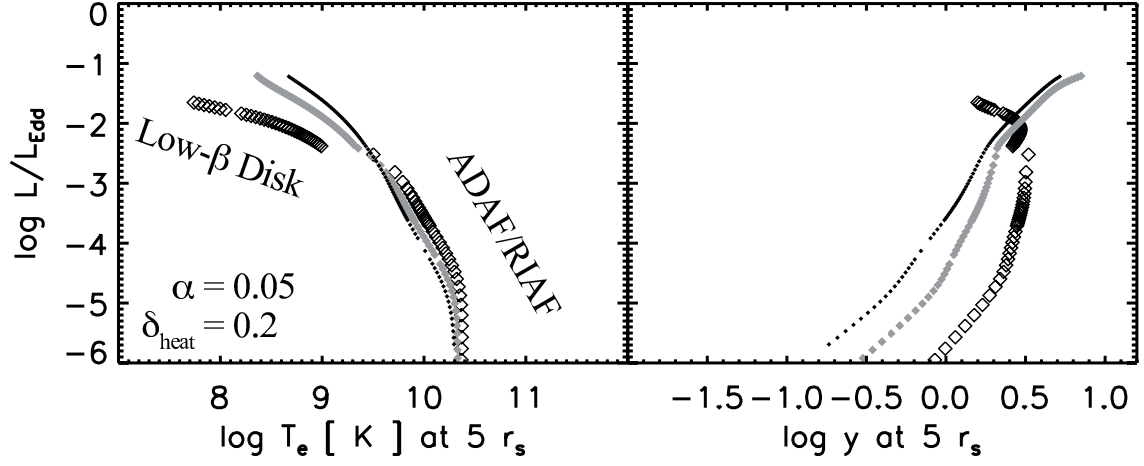


Fig. 12. Relation between T_e (left), and y (right) at $\varpi = 5r_s$ versus L . The disk parameters are $\alpha = 0.05$, $\delta_{\text{heat}} = 0.2$, $\zeta = 0.90$ (black), $\zeta = 0.75$ (gray), and $\zeta = 0.50$ (open diamond).

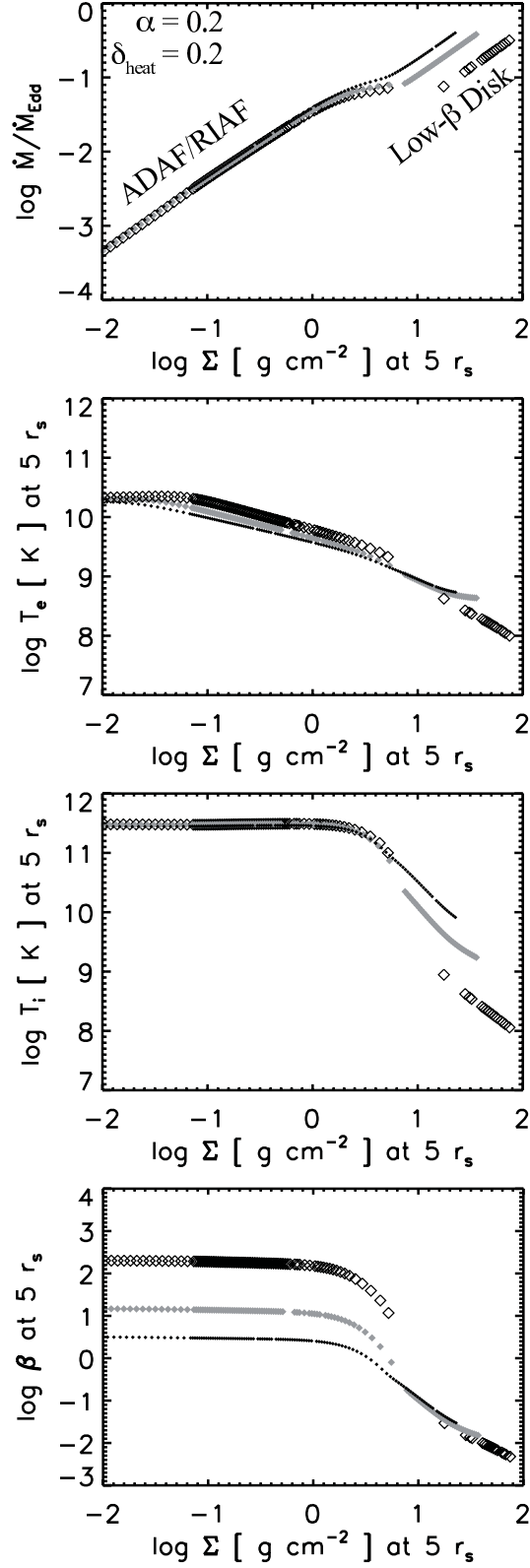


Fig. 13. Relation between Σ versus \dot{M} (top), T_e (second), T_i (third), and β (bottom) at $\varpi = 5r_s$. The disk parameters are $\alpha = 0.2$, $\delta_{\text{heat}} = 0.2$, $\zeta = 0.90$ (black), $\zeta = 0.75$ (gray), and $\zeta = 0.50$ (open diamond).

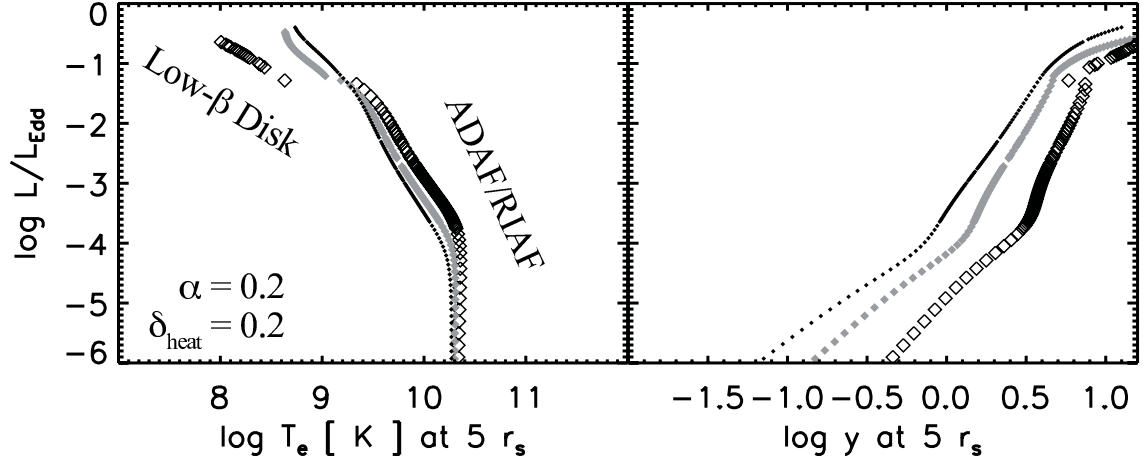


Fig. 14. Relation between T_e (left), and y (right) at $\varpi = 5r_s$ versus L . The disk parameters are $\alpha = 0.20$, $\delta_{\text{heat}} = 0.2$, $\zeta = 0.90$ (black), $\zeta = 0.75$ (gray), and $\zeta = 0.50$ (open diamond).

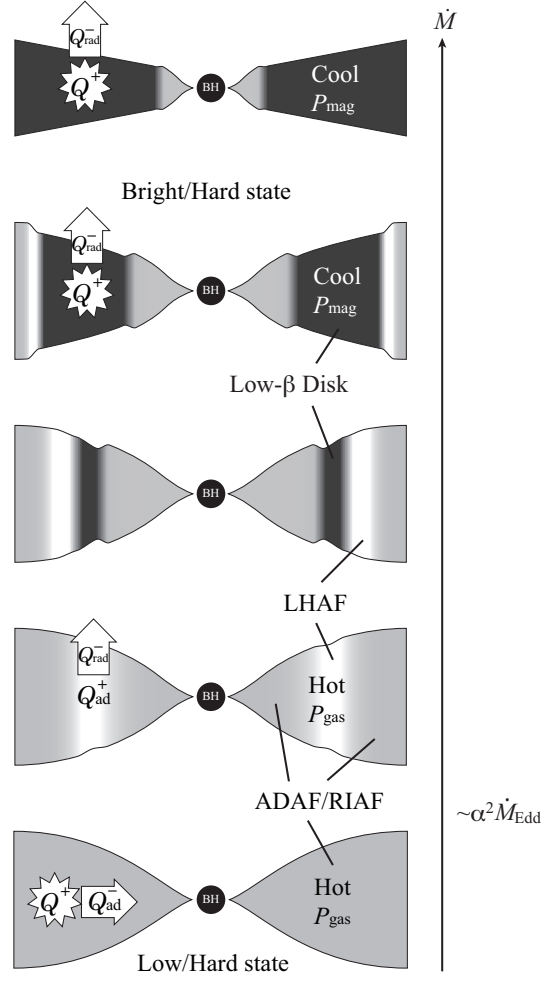


Fig. 15. Schematic pictures of configuration of accretion disks for various mass accretion rates. ADAF/RIAF regions are denoted by gray, LHAF regions by white, and low- β disk regions by black. The bottom panel shows the low/hard state at a low mass accretion rate. The top and second panels show the bright/hard state at high mass accretion rates. The middle panels show intermediate states during the transition from the ADAF/RIAF to the low- β disk, in which the LHAF appears.

Table 1. Disk parameters, luminosity, and radius of critical point

α	ζ	δ_{heat}	$\ell_{\text{in}}/(cr_s)$	$\dot{M}/\dot{M}_{\text{Edd}}$	L/L_{Edd}	r_{crit}/r_s	Type
0.05	0.90	0.2	1.4083924375	2.089×10^{-3}	1.430×10^{-4}	2.4443618	ADAF/RIAF
			1.5674186805	8.043×10^{-3}	1.450×10^{-3}	2.2445909	Critical ADAF/RIAF
			1.7231616728	1.224×10^{-2}	5.079×10^{-3}	2.1117202	LHAF
			1.7794718322	2.246×10^{-2}	1.241×10^{-2}	2.0844964	Low- β disk
			1.8124371548	5.984×10^{-2}	3.856×10^{-2}	2.0794780	Extremely Low- β disk
0.2	0.90	0.2	0.5974897133	3.993×10^{-3}	2.965×10^{-4}	4.8020671	ADAF/RIAF
			0.8908277177	5.712×10^{-2}	1.149×10^{-2}	3.1304441	Critical ADAF/RIAF
			1.4083890398	1.202×10^{-1}	9.244×10^{-2}	2.3096968	LHAF
			1.4445944039	1.445×10^{-1}	1.209×10^{-1}	2.3014862	Low- β disk
			1.5259917051	3.631×10^{-1}	3.622×10^{-1}	2.3316265	Extremely Low- β disk
0.05	1.00	0.2	1.3491502072	2.089×10^{-3}	1.522×10^{-4}	2.2885442	ADAF/RIAF
			1.6082077453	1.546×10^{-2}	5.102×10^{-3}	1.9937257	LHAF
			1.6680056446	2.353×10^{-2}	1.051×10^{-2}	1.9548674	Low- β disk
0.05	0.75	0.2	1.4389894702	2.089×10^{-3}	1.298×10^{-4}	2.5295339	ADAF/RIAF
			1.8135734019	8.830×10^{-3}	4.700×10^{-3}	2.2610183	LHAF
			1.8371197818	2.046×10^{-2}	1.259×10^{-2}	2.2653863	Low- β disk
0.05	0.50	0.2	1.4722433799	3.162×10^{-3}	1.954×10^{-4}	2.5178226	ADAF/RIAF
			1.8419696927	6.992×10^{-3}	4.181×10^{-4}	2.5116158	LHAF
			1.8441905224	1.564×10^{-2}	9.605×10^{-3}	2.5183405	Low- β disk